Experiments on the dynamics of waves on gravity-driven viscous film flows

Von der Fakultät für Ingenieurwissenschaften
der Universität Bayreuth
zur Erlangung der Würde eines
Doktor-Ingenieurs (Dr.-Ing.)
genehmigte Dissertation

von

Dipl.-Phys. Daniel Reck

aus

Forchheim in Oberfranken

Erstgutachter: Professor Dr. Nuri Aksel
Zweitgutachter: Professor Dr. Alexander Oron
Tag der mündlichen Prüfung: 19.07.2016

Lehrstuhl für Technische Mechanik und Strömungsmechanik
Universität Bayreuth
2016

Abstract

A gravity-driven viscous film flow consists of a layer of a viscous fluid that flows down an inclined or vertical substrate. The most simplified case appears, if the substrate is considered as perfectly flat without any roughness and of infinite extend in both directions. Then the Navier-Stokes equations can be solved analytically and the well known Nusselt solution with its parabolic velocity profile is at hand. Unfortunately, in real systems, like the lachrymal flow in the eye, glaciers, avalanches or a water film on a sloped road caused by heavy rain, this case does not apply. There is always some kind of roughness or undulation of the substrate involved that influences the behavior of the flow. Also those systems are not of infinite extend and so boundaries, e.g. side walls, have to be accounted for. Depending on their exact nature, these additional factors can have a major impact on the steady state of gravity-driven film flows.

If the volume flux of a film flow exceeds a certain threshold, waves appear at the free surface. These waves are the reaction of the system to disturbances, like e.g. ambient noise or external forcing. They grow or shrink on their way downstream and develop different wave shapes, depending on the properties of the steady flow and the external forcing. Both the onset of the free surface waves and their evolution on their way down the substrate are heavily impacted by the substrate undulations and the nature of the initial disturbances. It is of imperative importance for technical applications, e.g. coating, heat exchangers or falling film reactors, to know how exactly free surface waves can be influenced.

The present dissertation shows experimentally, how different substrate topographies affect the wave dynamics on film flows. For this, three substrates were used, whose periodic topographies had the same wavelength and amplitude, but diverse shapes: sinusoidal, saw-tooth-like and rectangular. Systematic measurements of the wave dynamics with different external forcing frequencies and amplitudes were carried out and referred to measurements of flows over a flat

substrate. Both the growth rate at the initial stages of the wave evolution and the saturation amplitude at later stages are significantly increased by the substrate's corrugations. On the other hand, the exact shape of the topography plays only a minor role.

Additionally, this work deals with experiments on the dynamics of solitary waves. Previous publications defined solitary waves as wave trains with a long area of flat film flow between the waves. Here, "truly solitary waves" were generated by perturbing the steady film flow with exactly one period of a sinusoidal disturbance. Without preceding and succeeding waves, the solitary wave can attune freely not only in the direction perpendicular to the flow, but also parallel to it. The influence of different periods and amplitudes of these disturbances was measured systematically. The results show that there is an interdependency between the amplitude and length of the waves: The shorter (longer) the waves become, the higher (lower) becomes their amplitude. At the end of the measurement channel, all measured waves on the same film flow tend to a similar amplitude and length. Also the waves' velocity does not depend linearly on the waves' amplitude, but rather quadratically.

A higher wave amplitude also means a higher velocity of a fluid particle at the free surface of the waves, since it is then farther away from the substrate. The wave's velocity grows with its amplitude, too. Streamline portrays of large solitary waves reveal that the velocity of the fluid at the free surface can be higher than the wave velocity. The waves do not break, but exhibit recirculation areas underneath the free surface, if the waves surpass a critical amplitude. This is of special interest in heat exchanger applications, since recirculation areas are known to enhance heat transfer in the cross direction.

Zusammenfassung

Eine schwerkraftgetriebene Filmströmung besteht aus einer Fluidschicht, die einen geneigten oder senkrechten Untergrund hinabfließt. Der einfachste Fall liegt vor, wenn der Untergrund als perfekt flach, ohne jede Rauigkeit und als in beide Raumrichtungen unendlich ausgedehnt angesehen wird. Dann können die Navier-Stokes-Gleichungen analytisch gelöst werden, mit der bekannten Nusseltlösung und ihrem parabolischen Geschwindigkeitsprofil als Endresultat. Leider ist dieser Fall auf reale Systeme wie z.B. die Tränenflüssigkeit in den Augen, Gletscher, Lawinen oder einen Wasserfilm auf einer abfallenden Straße nach starkem Regen nicht anwendbar. Es ist immer eine Art von Rauigkeit oder Unebenheit des Untergrunds vorhanden, die das Verhalten der Strömung beeinflusst. Auch sind diese Systeme nicht unendlich ausgedehnt und somit müssen Grenzen, z.B. Seitenwände, berücksichtigt werden. Je nach ihrer genauen Natur können diese zusätzlichen Faktoren einen bedeutenden Einfluss auf die stationäre schwerkraftgetriebene Filmströmung haben.

Falls der Volumenstrom einer Filmströmung einen bestimmten Schwellwert überschreitet, entstehen an der freien Oberfläche Wellen. Diese Wellen sind die Reaktion des Systems auf Störungen wie z.B. Rauschen aus der Umgebung oder externe Anregung. Sie wachsen oder schrumpfen während sie den Strömungskanal herunterfließen und entwickeln unterschiedliche Formen, abhängig von den Eigenschaften der stationären Strömung und von der Art der externen Anregung. Sowohl die Entstehung der Oberflächenwellen als auch deren Entwicklung auf ihrem Weg stromabwärts werden stark von Unebenheiten des Untergrunds und der Natur der ursprünglichen Störung beeinflusst. Für technische Anwendungen ist es ungeheuer wichtig zu wissen, wie genau die Oberflächenwellen manipuliert werden können.

Die vorliegende Dissertation zeigt anhand von Experimenten, wie sich verschiedene Untergrundtopografien auf die Wellendynamik von Filmströmungen

auswirken. Dafür wurden drei Untergründe benutzt, deren periodische Topografien die gleiche Wellenlänge und Amplitude, aber unterschiedliche Formen hatten: sinusförmig, sägezahnförmig und rechteckig. Systematische Messungen der Wellendynamik mit verschiedenen externen Anregungsfrequenzen und Anregungsamplituden wurden ausgeführt und auf die Messungen über einen flachen Untergrund bezogen. Sowohl die Wachstumsraten während der Anfangsphase der Wellenentwicklung als auch die Sättigungsamplitude während späterer Phasen sind durch die Unebenheit des Untergrunds deutlich erhöht. Andererseits spielt die exakte Form der Topografie nur eine untergeordnete Rolle.

Des Weiteren beschäftigt sich diese Arbeit mit Experimenten, welche die Dynamik von Einzelwellen untersuchen. Bisherige Publikationen definierten Einzelwellen als Wellenzüge, deren Wellen durch einen langen, flachen Film getrennt sind. Hier wurden nun „wahre Einzelwellen" generiert, indem die stationäre Filmströmung durch genau eine sinusförmige Störung angeregt wurde. Ohne vorangehende und nachfolgende Welle konnte sich die Einzelwelle nicht nur senkrecht zur Strömungsrichtung frei entwickeln, sondern auch parallel dazu. Der Einfluss verschiedener Störungsperiodendauern und Störungsamplituden wurde systematisch gemessen. Die Ergebnisse zeigen, dass sich die Länge und Höhe der Wellen gegenseitig beeinflussen: Je kürzer (länger) die Wellen werden, desto größer (kleiner) wird ihre Amplitude. Am Ende des Messkanals tendieren alle vermessenen Wellen über die gleiche Filmströmung gegen eine ähnliche Amplitude und Länge. Auch hängt die Geschwindigkeit der Wellen nicht linear von ihrer Amplitude ab, sondern quadratisch.

Eine größere Wellenamplitude bedeutet auch eine höhere Geschwindigkeit eines Flüssigkeitsteilchens an der freien Oberfläche der Wellen, da dieses dann weiter weg vom Untergrund ist. Genauso wird die Geschwindigkeit der Wellen mit ihrer Amplitude größer. Stromlinienbilder von großen Einzelwellen zeigen, dass die Geschwindigkeit der Flüssigkeit an der freien Oberfläche höher sein kann als die Wellengeschwindigkeit. Die Wellen brechen aber nicht, sondern es bilden sich Rezirkulationsgebiete unterhalb der freien Oberfläche, wenn die Wellen eine kritische Amplitude überschreiten. Dies ist von besonderem Interesse für Wärmetauscher, da Rezirkulationsgebiete bekanntermaßen den Wärmetransport in Querrichtung steigern.

Contents

1 Introduction

When a layer of a viscous fluid flows down an inclined or vertical substrate, this flow is called a gravity-driven viscous film flow. It appears in many different ways in nature: A water film on a sloped road during heavy rain, the flow of the lachrymal fluid in the eye and the movement of avalanches [1], glaciers [2], debris or lava are just a few examples. A rich variety of waves can form at the free surface of the liquid film and their dynamics heavily influence the function of different technical apparatuses: For example in coating applications [3–5], it is imperative to suppress the waves in order to obtain a smooth surface on the coated device. On the other hand, for falling film heat exchangers and reactors, free surface waves enhance heat transfer [6, 7] and so it is very important to control the properties of the waves in order to control the thermal transmission. This led to a very lively interest in the scientific community and a large number of publications were devoted to gravity-driven film flows and their wave dynamics.

1.1 The steady state of gravity-driven film flows

In 1916, Wilhelm Nusselt [8] solved the Navier-Stokes equations analytically for a film flow over a flat substrate of infinite extent. He found a quadratic dependency of the velocity on the distance from the substrate under the following predeterminations: The flow was assumed to be steady, its velocity field to be unidirectional and parallel to the substrate, the magnitude of the velocity to be only dependent on the distance from the substrate and the shear stress at the free surface to be zero. These assumptions exclude several features that are often crucial in real systems, e.g. intentional or unintentional roughness and undulations of the substrate or effects induced by the side walls.

The no-slip condition and capillary rise at the side walls of an inclined channel

lead to three-dimensional features of both the free surface shape and the velocity field of the film flow. If, due to the capillary rise, the film at the side walls is considerably thicker than in the middle of the channel, a pronounced velocity overshoot near the side walls was found experimentally and numerically [9] as well as analytically [10]. By further thinning the film, a rupture of the film in the middle of the channel marks the transition from a film to a corner flow [11]. Because of the no-slip condition, the liquid's velocity must be zero directly at the side walls.

Already very small (compared to the film thickness) single undulations (e.g. small particles) on a substrate can have a decisive impact on the free surface shape of a film flow, as shown semi-analytically by Pozrikidis and Thoroddsen [12] for a creeping flow. Also the influence of bumps or dents, approximated by step-up-step-down/step-down-step-up geometries were investigated by a lubrication approximation [13], analytically via a Green function [14], by using a boundary integral method [15] and experimentally [16]. The influence of capillarity on the free surface shape was subject to analytical, numerical and experimental work by Aksel [17]. The authors of [12–17] found a free surface depression near step-ups of the topographies, and ridges near step-downs. The magnitude of these features depends on the width, depth and steepness of the mounds or trenches and on the capillary pressure at the free surface of the film flow. Scholle and Aksel proved analytically [18] that for creeping film flows, the volumes of depression and elevation of the free surface caused by a trench, have to be equal.

The influence of periodical substrate corrugations on the steady state of gravity-driven viscous film flows was researched extensively. Concerning the free surface, the undulated substrate provokes an undulated free surface. If a creeping flow is considered, the amplitude of the free surface's undulation decreases with an increasing film thickness [19–21]. On the other hand, a laminar film flow with significant inertia exhibits a different reaction to substrate undulations: The amplitude of the free surface undulations increases with the Reynolds number (which is a measure for the influence of inertia), until a maximum (resonance) is reached and then decreases again [20, 22, 23]. The Reynolds number, where this maximum is located, depends on the geometry of the substrate, the film thickness and the hydrostatic and capillary pressure. Since the nonlinear

terms in the governing equations were omitted, this is only valid for a small substrate waviness. A higher waviness causes higher harmonics in the free surface's shape and the resonance is shifted to higher Reynolds numbers [24–27]. Also generally, the resonance is not influenced by the exact shape (e.g. rectangular or sinusoidal) of the geometry [28]. By varying the inclination angle of the substrate, Wierschem and Aksel [29] found not only resonant waves, but also shocks, humps and surface rollers. The other way round, it was proven that an unknown substrate geometry can be calculated from a known free surface shape [30–32] or velocity [33].

Additionally to the free surface, substrate corrugations also change the velocity field of a film flow. For a Stokes flow, Pozrikidis [19] reported on flow reversal in the troughs of different sinusoidal undulations, by using a boundary integral formulation. These eddies are also formed, when inertia is considered, as shown by Trifonov [22], who solved the steady Navier-Stokes equations numerically. So when do these eddies appear? Wierschem et al. [34] (experimentally) and Scholle et al. [35] (analytically) studied a creeping flow and found the film thickness (and not the Reynolds number) to be the critical parameters for the onset of eddies in the troughs. This threshold depends on the waviness of the substrate. If inertia is involved, the eddy size increases and the eddy becomes tilted towards the upstream position [36, 37]. This leads to competing effects of geometry and inertia on the local flow structure of film flows [38]. Eddies can also appear on the crest of a rectangular undulation [25]. The vortical structures enhance the heat transfer between the substrate and the free surface of the liquid film [39].

Wierschem et al. [40] showed that the shape of the free surface can impact the formation of the eddies. When the free surface is strongly curved or even a hydraulic jump appears through the resonant effects described above, eddies can be suppressed at certain Reynolds numbers.

1.2 The stability of gravity-driven film flows

Since gravity-driven film flows are bounded by a free surface and not a rigid wall, they are very susceptible to disturbances. Experiments, carried out by

Pjotr and Sergei Kapitza [41, 42], revealed that a film flow over a flat substrate becomes unsteady and waves appear spontaneously at its free surface, if a certain volume flux threshold is exceeded. This led to analytical computations by Yih [43] and Benjamin [44], who adapted the Orr-Sommerfeld equation [45–47] to film flows, and experiments by Liu et al. [48]. They found that a film flow becomes unstable to infinitely long waves, when the Reynolds number surpasses a critical value of $Re_c = 5/4 \times \cot \alpha$. Hence the stability map which represents the neutral curve in the wave number/Reynolds number plane, exhibits a long-wave type instability.

The computations in the previous paragraph were done for the idealized case of an infinitely broad channel without side walls. Taking side walls with the no-slip-condition and the capillary rise into account, a stabilizing effect [49, 50] of the side walls was found along with a transition from a long-wave to a short-wave instability [51]. The significance of those features depends on the Kapitza number (which is a measure for the influence of the surface tension), the distance from the side walls and the contact angle between the fluid and the side walls.

The stability of gravity-driven film flows also changes, if weak substrate undulations are present. First analytical results, obtained by Wierschem and Aksel [52], indicate that the flow is stabilized by undulations of moderate amplitude and long wavelength compared to the film thickness. The stability behavior is still of the long-wave variety, as for the flow over flat substrates. These findings were confirmed analytically [53], numerically [54] and experimentally [26, 27, 53]. It is also stated in these papers that the stabilizing effect of a substrate can be increased by steepening the undulations. Numerical investigations by Trifonov [55–57], who used either integral approaches or the Navier-Stokes equations in their full statement, revealed that a flow is stabilized by corrugations, if they generate a significant increase of the mean film thickness compared to a Nusselt flow.

By carrying out numerical calculations, D'Alessio et al. [58] and Tseluiko et al. [59] found that the flow can be stabilized or destabilized by steep substrate undulations, depending on the amplitude and wavelength of the substrate and the surface tension of the fluid. Heining and Aksel [60] were the first to report on a completely new stability phenomenon of a film flow over strongly

corrugated substrates: In their analytical and numerical study, they used an integral boundary layer model to reveal a disjointed stability map. The authors discarded the rather unexpected finding of separated unstable islands as an artifact caused by the linearization of the problem. Their existence, however, could be confirmed experimentally by Pollak and Aksel [61] and numerically by Trifonov [62], who used the full Navier-Stokes equations. Experiments by Schörner et al. [28] also revealed that the qualitative appearance of the stability map can generally not be changed by the substrate's specific shape (e.g. rectangular, saw-tooth-like or sinusoidal), without changing the wavelength or amplitude of the undulations. Through extensive experimental work, Schörner et al. [63] were able to unveil the influence of the fluid's viscosity and the substrate's waviness and inclination angle on the stability. They were able to link the first unstable island in the stability maps to the resonance phenomenon of the steady state film flow (section 1.1). Pollak and Aksel [61] Cao et al. [64], Trifonov [62] and Schörner et al. [63] found a transition from a long-wave type instability to a short-wave type by either increasing the inclination angle of the substrate or by decreasing the viscosity of the fluid.

1.3 The wave dynamics on gravity-driven film flows

The dynamics and evolution of waves that appear due to the instability of the film flow (section 1.2) or external forcing were examined elaborately in the literature for flows over flat substrates. Several models were derived for the influence of a non-zero wave amplitude on the evolution of free surface waves, e.g. [65–74]. Chang and Demekhin cover this topic in their book "Complex wave dynamics on thin films" [75]. Also extensive numerical and experimental studies [48, 76–88] have been carried out. They focus on the evolution of the waves down a channel and on the steady state these waves reach eventually due to nonlinear effects. A rich variety of waves can appear which were categorized into families by Chang et al. [89]. Craster and Matar [90] reviewed this topic in detail and reported the consensus that mostly, two types of waves are found in the regarded systems: a) Nearly sinusoidally shaped waves of comparably small wavelength and wide peaks, and b) solitary structures which are separated by a large area of smooth film flow and have a high narrow crest and can exhibit

multiple peaks. These solitary waves are often preceded by small ripples, called capillary waves. The steady state, sinusoidal and solitary waves reach, can become unstable itself and break up into three-dimensional structures [91–94].

Very little is known about the influence of substrate undulations on the wave dynamics on gravity-driven film flows. Some publications dealt numerically or experimentally with the wave evolution on the free surface of a film flow over undulated substrates [27, 54, 55, 59, 95]. They described the waves as a superposition of the steady state waves and the proceeding unsteady waves. This leads to a dependency of the unsteady waves' amplitude on the position inside a substrate's wavelength. Argyriadi et al. [27] showed that the saturation state amplitude of free surface waves over undulated substrates is higher than of waves over a flat substrate under otherwise equal circumstances.

1.4 Scope of this dissertation

The scope of this dissertation is twofold. One part is devoted to a better understanding of the dynamics of unsteady free surface waves on gravity-driven film flows. Especially the influence of different substrate undulations is scrutinized and compared to results for a flat substrate and existing knowledge in the literature. For a fixed steady state film flow, the waves were investigated systematically by adding unsteady sinusoidal waves of different frequency and amplitude and measuring their evolution down a channel. Additionally to the flat substrate that was used as a reference, three undulated substrates with the same wavelength and amplitude, but different shapes (sinusoidal, saw-tooth-like and rectangular), were inserted into the channel.

The second part deals with the dynamics of solitary waves over a flat substrate. Most publications consider wave trains, whose humps are separated by an area of smooth free surface as solitary waves. The present work investigates "truly solitary waves", who are not part of a wave train. Waves of different heights and lengths were generated and again the evolution of these waves down a channel was measured and analyzed regarding their amplitude, speed, length and shape. Also the flow field underneath large solitary waves was portrayed.

The dissertation is structured as follows: Chapter 2 describes the studied sys-

tem and the measurement techniques that capture the properties of the steady state (basic) flow and of the unsteady continuous and solitary waves. Chapter 3 deals with the mathematical formulation of the steady film flow and linear free surface waves as well as with different model equations for nonlinear free surface waves. Chapter 4 comprises the presentation and discussion of the experimental results which are compared to numerical calculations. The dissertation closes with concluding remarks in chapter 5.

2 Studied systems and measurement techniques

2.1 Basic flow

The basic flow was defined as an undisturbed, steady, two-dimensional, gravity-driven film flow down an open channel which was inclined by α relative to the horizontal (figure 2.1). It can be described by its free surface position in z-direction $h_0(x)$ and its velocity field $\vec{u}(x, z)$. These quantities depend on the liquid's kinematic viscosity ν and surface tension σ, the two-dimensional flow rate $\dot{Q}$ (calculated from the volume flux $\dot{V}$), the inclination angle α and the topography of the channel's inlay.
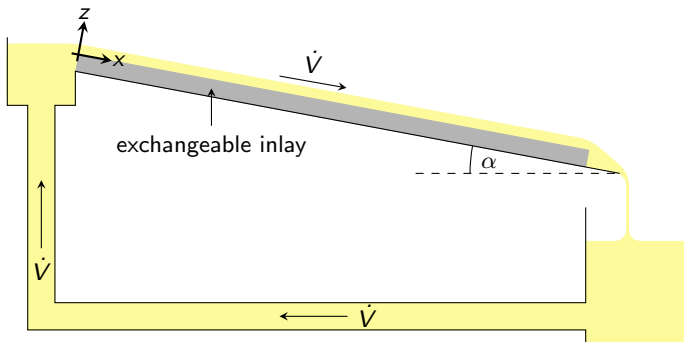

Figure 2.1: The flow circuit that was used to set up the basic film flow.

2.1.1 Topographies and inclination angle

The flow over four different substrate topographies was investigated by exchanging the inlays in the channel: the flat (S_0), sinusoidal (S_1), saw-tooth-like (S_2) and rectangular (S_3) shapes that are shown in figure 2.2. The undulated substrates shared the same amplitude $a_{sub} = 4\,\mathrm{mm}$ and wavelength $L_{sub} = 20\,\mathrm{mm}$. All substrates had the same width $w_{sub} = 170\,\mathrm{mm}$ and were bordered in y-direction by transparent side walls. Due to the manufacturing process, the inlays S_0, S_1, S_2 and S_3 had different counts of waves $N_{sub} = 67, 55, 43, 61$ and hence different lengths $l_{sub} = N_{sub} \times L_{sub} = \{1340, 1100, 860, 1220\}\,\mathrm{mm}$.

The channel with the exchangeable inlay was mounted on a structure which was designed to enable the continuous variation of the inclination angle α. This angle was measured with a *Mitutoyo Pro 360 Digital Protractor 950-315* with an accuracy of $\pm 0.1\,^\circ$. The x-y-plane of the coordinate system was defined by the surface of the flat inlay. With a water balance, the y-axis was positioned exactly parallel to the horizontal. Hence, the x-axis was inclined by α with respect to the horizontal.
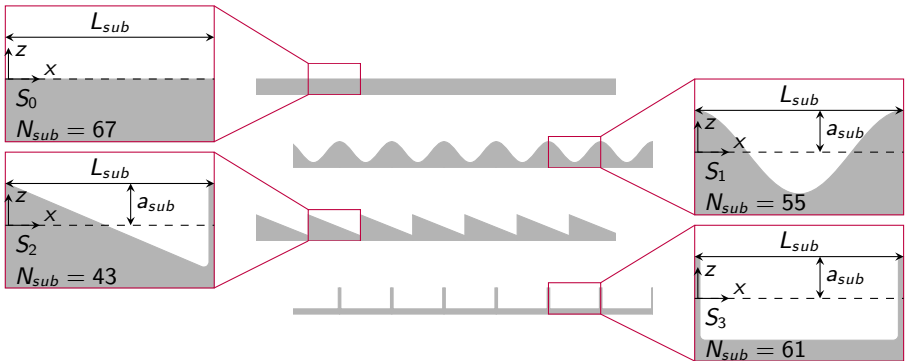

Figure 2.2: The topographies used for the measurements of the wave dynamics: flat (S_0), sinusoidal (S_1), saw-tooth-like (S_2) and rectangular (S_3). A substrate consisted of N_{sub} repetitions of the enlarged shapes on the left and right hand side. Each sketch in the middle represents a part of one of the substrates.

2.1.2 Two-dimensional flow rate

The two-dimensional flow rate $\dot{Q}$ was calculated from the three-dimensional volume flux $\dot{V}$ through the flow circuit (figure 2.1) and the channel's width w_{sub} which was $(170 \pm 1)\,\text{mm}$ for all experiments:

$$\dot{Q} = \dot{V}/w_{sub}. \tag{2.1}$$

With this equation, it is assumed that $\dot{Q}$ is constant over the width of the channel. Because of the no-slip condition and capillary rise at the side walls, $\dot{Q} = \dot{Q}(y)$ is a function of y. For flat topographies, Scholle and Aksel [10] computed $\dot{Q}(y)$ analytically and showed that the flow rate $\dot{Q}(w_{sub}/2)$ at the channel's center deviates with less than $1\,\%$ from $\dot{V}/w_{sub}$ for the case presented in this dissertation. Unfortunately, no such work has been done for undulated topographies. It was assumed without prove that a similar behavior is at hand.

In order to produce the steady basic flow, a constant volume flux $\dot{V}$ was provided by pumps from *PF Jöhstadt* type *SK 80S/4* and type *SK 90L/4*. During an experiment, $\dot{V}$ was measured continuously by ultrasonic flow meters from *Deltawave* type *XUC-F*. In figure 2.3 can be seen that fluctuations around the constant value of $\dot{V}$ were less than $\pm 3\,\text{cm}^3/\text{s}$.
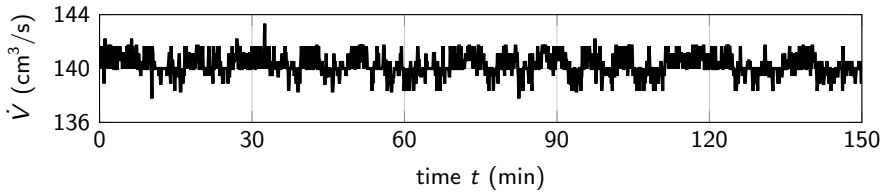

Figure 2.3: The measured volume flux $\dot{V}$ for the duration of a wave dynamics experiment.

By solving the Navier-Stokes equations, as shown in various text books, e.g. [96], the Nusselt film thickness d_n and free surface velocity u_s for the flow over the flat substrate can be calculated:

$$d_n = \sqrt[3]{\frac{3\nu\dot{V}}{gw_{sub}\sin\alpha}}, \tag{2.2}$$

$$u_s = \sqrt[3]{\frac{9\dot{V}^2 g\sin\alpha}{8\nu w_{sub}{}^2}}. \tag{2.3}$$

Here, $g = 9.81\,\mathrm{m/s^2}$ is the gravitational constant and ν stands for the kinematic viscosity which will be explained in section 2.1.3. The film thickness and free surface velocity of flows over undulated substrates cannot be calculated exactly from the Navier-Stokes equations.

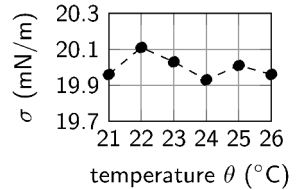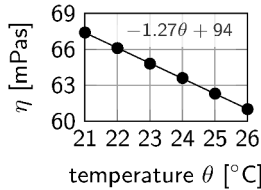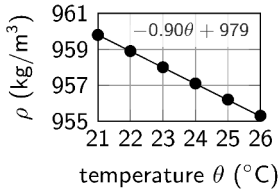### 2.1.3 Surface tension, viscosity and density

Within the experiments, two different Newtonian liquids were used. Both were silicon oils from *Elbesil*, denoted as *Elbesil 65* and *Elbesil 100*. Their density ρ and dynamic viscosity η were measured and yielded the kinematic viscosity $\nu = \eta/\rho$. Also the surface tension σ was determined. The following devices were utilized:

A Mohr-Westphal-Balance from *Kern* was used to obtain the density of the liquids. The temperature of the balance was set by a thermostat from *Lauda*. The dynamic viscosity of the oils was determined by an Ubbelohde capillary viscosimeter from *Schott* which was dipped into a water bath, whose temperature was controlled by a thermostat, also from *Schott*. The surface tension was measured with a ring-tensiometer from *Lauda*. A thermostat from *Lauda* set the temperature of the fluid.

Since ρ, η and hence ν are temperature sensitive, the liquids' properties were measured in a temperature range between $21\,^\circ\mathrm{C}$ and $26\,^\circ\mathrm{C}$ in intervals of $1\,^\circ\mathrm{C}$. The results are shown in figure 2.4, with a linear function fitted to the data of ρ and η. The surface tension σ does not show a distinct dependence on the temperature, but fluctuated around a constant value. A thermostat from *Haake* and a *PT-100* temperature sensor, controlled by a custom made *LabView*

program, secured a constant temperature $\theta = (23.0 \pm 0.2)\,°\text{C}$ during the wave dynamics experiments (figure 2.5). With this and the data from figure 2.4, the values of σ, ρ, η and ν could be calculated and are shown in table 2.1. The uncertainties of these results were obtained from the errors of the linear fit (for ρ and η) and from the fluctuations around the constant value of σ.
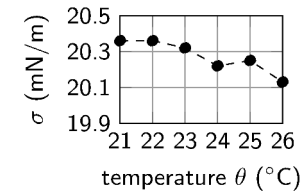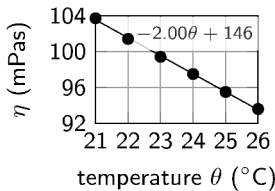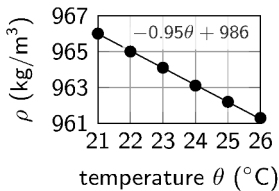
Elbesil 65:

Elbesil 100:

Figure 2.4: The density ρ, dynamic viscosity η and surface tension σ of both silicon oils. A linear regression line was fitted to the data of ρ and η.
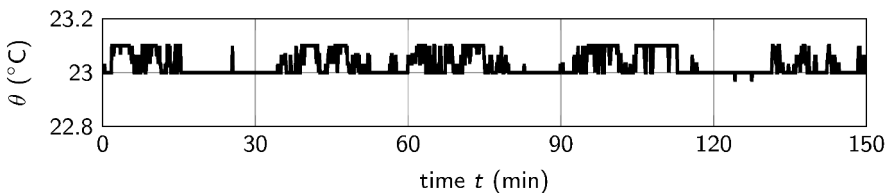
Figure 2.5: The measured temperature θ for the duration of a wave dynamics experiment.

	σ (mN/m)	ρ (kg/m^3)	η (mPas)	ν (mm^2/s)	Ka
Elbesil 65	20.0 ± 0.1	958.3 ± 0.2	64.8 ± 0.3	67.6 ± 0.3	3.54 ± 0.02
Elbesil 100	20.2 ± 0.2	964.2 ± 0.2	100.0 ± 0.4	103.7 ± 0.4	2.01 ± 0.02

Table 2.1: The fluid properties and the Kapitza number with their estimated errors for both silicon oils, at $\theta = (23.0 \pm 0.2)$ °C.

2.1.4 Dimensionless quantities

The values given in sections 2.1.1 through 2.1.3 only describe a very narrow parameter space. Using dimensionless quantities enables comparisons to cases, where different parameters were used. The most commonly used dimensionless numbers to describe film flows are the Kapitza and Reynolds number. The Kapitza number Ka describes the ratio of surface tension forces to inertial forces (Definition as in [75]):

$$Ka = \frac{\sigma}{\rho g^{1/3} \nu^{4/3}}. \tag{2.4}$$

The Kapitza number only depends on the liquid's properties (table 2.1) and not the flow itself. The Reynolds number

$$Re = \frac{u_s d_n}{\nu} \tag{2.5}$$

describes the ratio of inertial forces to viscous forces which depends on the characteristic velocity u_s and the characteristic length d_n of the flow. The characteristic length and velocity of the film flow over the flat substrate are its film thickness d_n and free surface velocity $u_s = u(d_n)$ (equations 2.2 and 2.3). Combining equation 2.5 with equations 2.1 through 2.3 yields

$$Re = \frac{3\dot{Q}}{2\nu}. \tag{2.6}$$

The characteristic length and velocity of a film flow over the strongly undulated substrates is not defined as easily. The first problem is that the flow field cannot be calculated exactly from the Navier-Stokes equations. Secondly, both the

local film thickness $d_{loc}(x)$ and the free surface velocity $u_{loc}(x)$ depend strongly on the position inside a substrates wavelength and hence on the x-coordinate. Consequently, also the Reynolds number, if computed from $u_{loc}(x)$ and $d_{loc}(x)$ would be a function of x. In order to have a globally valid Reynolds number, we chose to use the Reynolds number of the corresponding flow over the flat substrate with the same flow rate $\dot{Q}$ (equation 2.6). Since the Reynolds number is calculated from the two dimensional flow rate $\dot{Q}$, which in turn is derived from the three dimensional volume flux $\dot{V}$ and the channel's width w_{sub} (equation 2.1), and the kinematic viscosity ν, it also carries an uncertainty: $\Delta Re \leq 0.5$.

2.1.5 Measurement of the basic flow

The techniques described in this section and in section 2.2 were also used by Reck and Aksel in [95]. The position of the basic flow's free surface $h_0(x)$ was measured by the setup sketched in figure 2.6. The fluorescent dye *Quinizarin* from *Sigma Aldrich* was dissolved into the silicon oils and excited by a blue line laser from *Laser Components*, type *FP-L-450-40-10-F210*. The continuous wave radiation had the wavelength $\lambda_{blue} = 450\,\text{nm}$ and the power $P_{blue} = 40\,\text{mW}$. The laser was mounted above the middle of the channel width at its working distance $(210\,\text{mm})$ from the flow's free surface, in order to receive the narrowest line possible.
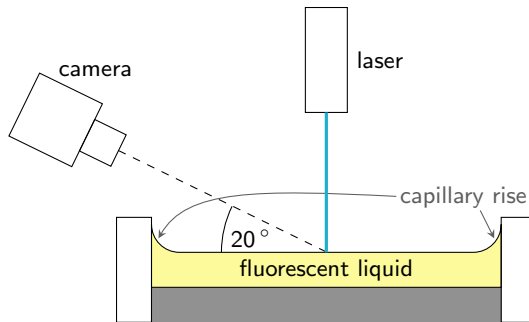

Figure 2.6: The experimental setup for the measurement of the free surface shape.

The length l_{blue} and width w_{blue} of the laser line was calculated from the data sheet provided by *Laser Components* [97]: $l_{blue} = 37 \, \text{mm}$, $w_{blue} = 0.25 \, \text{mm}$. The fluorescent liquid was recorded by a *CR600x2* camera from *Optronis* which was inclined by approximately $20\,^{\circ}$ with respect to the y-axis, to avoid the capillary rise at the side walls (figure 2.6). The perspective contortion was corrected by recording a calibration plate (figure 2.7) with the same camera and setup. The recorded free surface is displayed in figure 2.8, exemplarily for a flow over the sinusoidal substrate. An edge-detection algorithm was developed in *MATLAB*, in order to retrieve the free surface contour $h_0(x)$ of the basic flow as the boundary between the bright liquid and the dark air: First a Gaussian filter had to be applied, to get rid of high frequency noise. For every column of the recordings, the algorithm then calculated the first derivative of the brightness distribution (graphs in figure 2.8). The coordinate of its maximum was read out and with the help of the aforementioned calibration plate, it could be allocated to the position of the free surface in the x-z-coordinate system. This position was then defined as the location of the steady state free surface $h_0(x)$. The result is shown in figure 2.9. It was not necessary to measure the velocity field of the basic flow, because it was not needed to analyze and discuss the wave dynamics on the film flow.
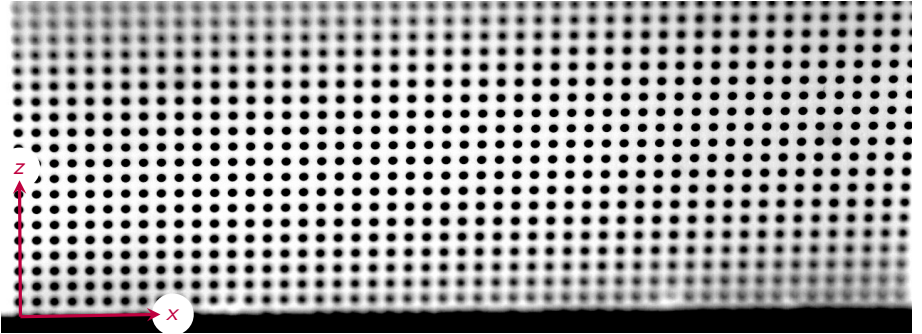

Figure 2.7: The calibration plate that was used to correct the perspective contortion. The dots have the diameter 0.25 mm and are 0.5 mm apart. So each pixel in the recorded images was allocated to a position in the x-z-coordinate system. The black stripe at the lowest part of the image is the surface of the flat substrate.
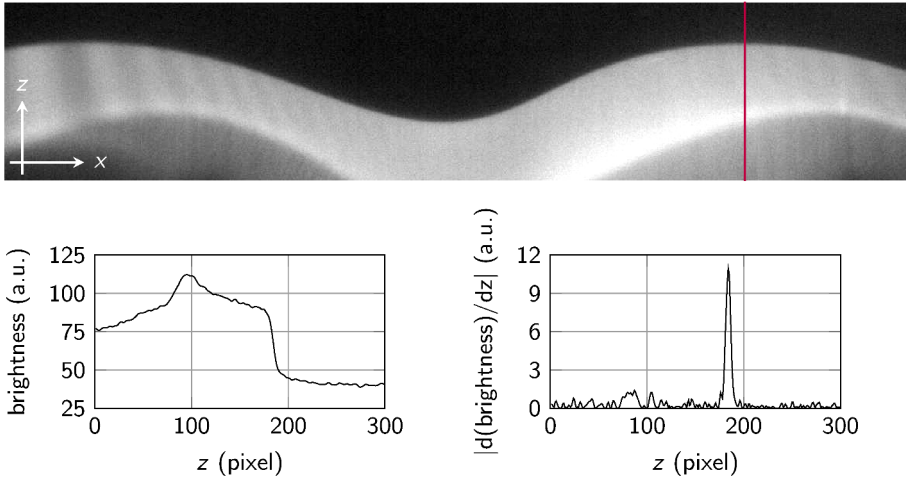
Figure 2.8: The flow over the sinusoidal substrate portrayed by the setup described in section 2.1.5. The free surface is the interface between the bright liquid and the dark air. The purple line marks the column of the recording, for which the brightness distribution and its derivative are plotted below.
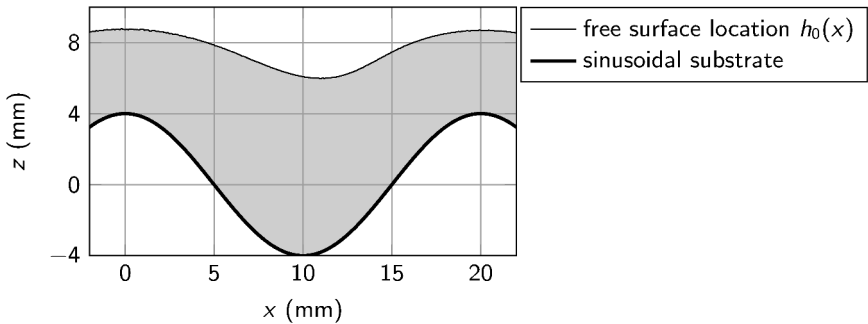

Figure 2.9: An example for the detected free surface location $h_0(x)$ for S_1 and the dimensionless parameters $Ka = 2.01$, $Re = 11.9$.

2.2 Wave dynamics

The goal of this dissertation is to describe the dynamics of both continuous and solitary waves which run over a gravity-driven film flow. It is important to distinguish them from the steady waves which occur due to the undulated substrates (figure 2.9). Those waves are part of the basic flow and were described in section 2.1.5.

2.2.1 Continuous waves

The continuous waves overlaid the basic flow with a non-steady addition whose shape is denoted as $h_c(x,t)$. The waves were described by their amplitude a_c, wave number k_c and phase velocity v_c. A paddle that was mounted at the inlet of the channel and driven by a direct current motor (figure 2.10) produced the waves. The paddle's up-and-down movement is described by

$$a_p(t) = a_{p,0} \cos\left(2\pi f_p t\right), \tag{2.7}$$

with f_p being the frequency and $a_{p,0}$ the amplitude of the paddle movement. The free surface shape $h(x,t)$ of the entire unsteady flow consisted of the steady basic flow and the unsteady continuous waves:
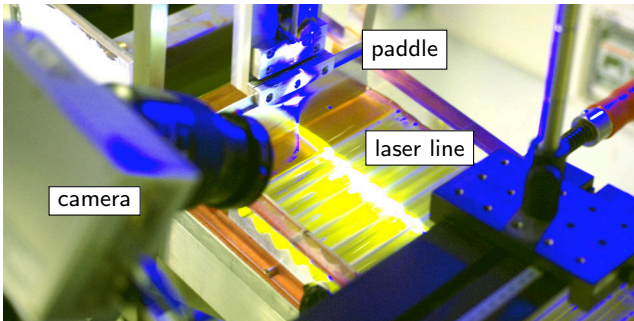
$$h(x,t) = h_0(x) + h_c(x,t). \tag{2.8}$$

Figure 2.10: Position of the paddle at the channel's inlet. Also visible: Camera and laser line. Reproduced with permission from [95]. ©2013, AIP Publishing LLC.

The shape $h(x,t)$ was recorded with the same setup as the basic flow's free surface shape $h_0(x)$ (section 2.1.5) with a frame rate of 200 frames per second. In total 1200 frames were taken. The same edge-detection algorithm as in section 2.1.5 then computed the free surface shape $h(x,t)$. In order to gather the unsteady continuous waves $h_c(x,t)$, the shape of the basic flow's free surface was subtracted from $h(x,t)$.

The whole channel was up to 67 times longer than the area recorded by the camera. In order to gain a reasonable resolution of the free surface's shape, it was not possible to portray the whole channel length at once. So the camera and laser were mounted on a traversing unit which was moved along the channel to record the free surface's shape in fragments which were as long as the substrate's wavelength $L_{sub} = 20\,\mathrm{mm}$. This length was convenient, because then the free surface shape of the basic flow repeats itself for all N_{sub} measurement positions. The size of an image in x-direction was about $x_c = 28\,\mathrm{mm}$, hence an overlap between adjacent recordings occurred. The layout of the setup made it impossible to access the first measurement position.
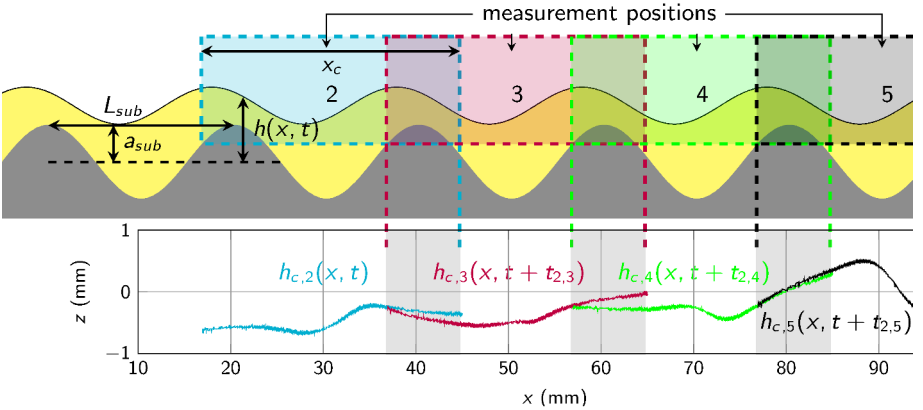

Figure 2.11: The sketch shows the uppermost part of the substrate S_1 with the measurement positions two through five. The recorded areas show overlaps to the adjacent ones. These were used to erase the mismatches between the fragments of the unsteady waves which are shown below, and join them together. Reproduced with permission from [95]. ©2013, AIP Publishing LLC.

After all fragments of the unsteady wave $h_{c,i}(x,t)$, $i = \{2, ..., N_{sub}\}$ had been obtained, they were joined together by the following procedure: Due to the overlap between the images of adjacent measurement positions, the right end of the recorded pictures at e.g. measurement position 2 showed the same part of the channel as the leftmost part of the recorded pictures at measurement position 3 (figure 2.11). The measurements at these two positions did not take place at the same time but with a delay of $t_{2,3}$. Because of the periodic nature of the waves produced by the paddle, the unsteady wave repeats itself after each period $1/f_p$. That means

$$h_{c,2}(x,t) = h_{c,2}\left(x, t + \frac{n}{f_p}\right) \tag{2.9}$$

and exemplarily for $x = 40\,\text{mm}$ (figure 2.11)

$$h_{c,2}(40\,\text{mm}, t) = h_{c,3}\left(40\,\text{mm}, t + \frac{n}{f_p}\right), \tag{2.10}$$

with n being a natural number. With our setup, it was not possible to set the time delay to $t_{2,3} = n/f_p$. Consequently, the fragments $h_{c,2}(x,t)$ and $h_{c,3}(x, t + t_{2,3})$ in figure 2.11 show a mismatch. That mismatch was erased by looking at both amplitude-time-curves at a certain position in the overlap region, e.g. $x = 40\,\text{mm}$. The curves $h_{c,2}(40\,\text{mm}, t)$ and $h_{c,3}(40\,\text{mm}, t)$ are plotted on the left hand side in figure 2.12 and show a slight phase difference $\tau_{2,3}$. The phase difference was then calculated by computing the Fast Fourier Transformation $\mathcal{F}(h_{c,2}(40\,\text{mm}, t))$ and $\mathcal{F}(h_{c,3}(40\,\text{mm}, t))$ with the built-in *MATLAB* function `fft()`. By plotting the imaginary parts $\mathcal{I}$ against the real parts $\mathcal{R}$ of the resulting functions (figure 2.12 right hand side), one can read out the phase difference $\varphi_{2,3}$ in radian measure and calculate the phase difference $\tau_{2,3}$ in seconds:

$$\tau_{2,3} = \frac{\varphi_{2,3}}{2\pi} \cdot \frac{1}{f_p}. \tag{2.11}$$

This was carried out for all points in the overlap area between positions 2 and 3 of figure 2.11. The accuracy of $\tau_{2,3}$ was improved by averaging over these points. Then the phase differences $\tau_{i,i+1}$ ($i = \{2, ..., N_{sub} - 1\}$) were calculated

for all overlap areas between the measurement positions. Since all fragments had to be in the same phase, all phase differences were referred to the same measurement position, i.e. the one for $i = 2$:
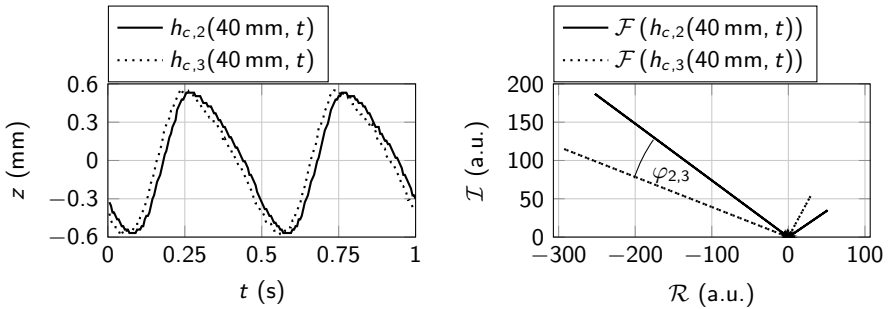
$$\tau_{2,i} = \sum_{j=2}^{i-1} \tau_{j,j+1}.$$ (2.12)

Figure 2.12: The graph on the left side shows the amplitude-time-curves at the same downstream distance from the inlet $x = 40\,\text{mm}$ for the measurements at positions two and three which have a slight phase difference. The phase difference $\varphi_{2,3}$ in radian measure can be read from the graph on the right hand side which displays the imaginary parts of the Fourier Transformations of the two amplitude-time-curves against their real parts.
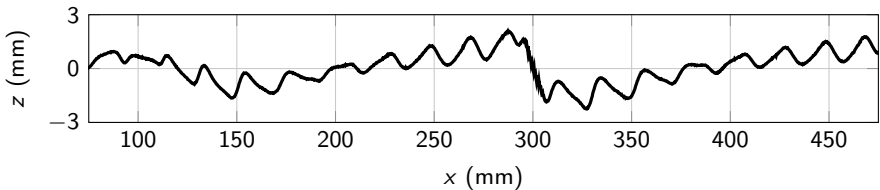

Figure 2.13: An example of the defragmented wave $h_c(x, t)$ for a part of the channel with the sinusoidal inlay S_1 at a random time. Reproduced with permission from [95]. ©2013, AIP Publishing LLC.

In the last step, all fragments were joined together by superposition:

$$h_c(x,t) = \sum_{i=2}^{N_{sub}} h_{c,i}(x, t + \tau_{2,i}). \tag{2.13}$$

An example for the resulting defragmented wave is shown in figure 2.13.

2.2.2 Solitary wave

A solitary wave $h_s(x,t)$ was characterized by its amplitude a_s, phase velocity v_s and full length at half maximum λ_s (defined as the distance between the front and tail of the wave at $a_s/2$). It was produced by a paddle which was mounted as in section 2.2.1, but now connected to a linear motor from *LinMot*. The paddle moved up and down in a sinusoidal motion (equation 2.7), and since only one solitary wave was required, the movement of the paddle stopped after one period $T_p = 1/f_p$.

Here, the basic flow was overlain by the solitary wave:

$$h(x,t) = h_0(x) + h_s(x,t) \tag{2.14}$$

The recording procedure is identical to section 2.2.1, but the defragmentation routine is different: Here, no periodic signal is present. So after one measurement position had been recorded, the camera and laser were moved to the next position. Then a new solitary wave, which was identical to the previous one, was produced and recorded by the camera at the new position. Due to the linear motor, it was now possible to set the time between the release of the wave and the start of the recording by the camera to exactly the same value. Consequently, no mismatch between the fragments of the measurement positions i and $i+1$ appeared and the fragments were simply joined together without the need to calculate a phase difference:

$$h_s(x,t) = \sum_{i=2}^{N_{sub}} h_{s,i}(x,t). \tag{2.15}$$

A plot of an exemplary defragmented solitary wave is shown in figure 2.14. The dynamics of solitary waves were only measured for film flows over the flat substrate S_0.
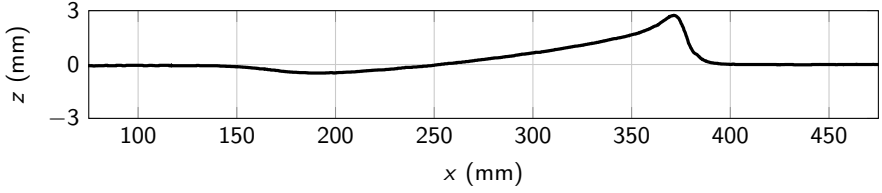
Figure 2.14: An example of the defragmented solitary wave $h_s(x, t)$ for a part of the channel with the flat inlay S_0 at a random time.

Additionally to the solitary wave's shape, the streamlines underneath the wave were recorded in a coordinate system (x', y, z) that moved with the wave's speed: $x' = x - v_s t$. The procedure was published in [98]: The moving coordinate system consisted of a camera *(The Imaging Source, DMK 41BU02/72BUC02)* to record the streamlines of the flow and a red line laser *(Laser Components, FP-L-635-30P-10-F210)* to illuminate the scattering particles in the fluid. Both were mounted on a slide which could move along a guide rail that was fastened parallel to the substrate in the channel. The slide was connected to a linear motor from *LinMot* which had a total range of 280 mm, thereof 112 mm were used for acceleration and 56 mm for deceleration. Consequently, the slide moved with a constant speed over a distance of 112 mm. The velocity of the coordinate system was set to a value between 500 mm/s and 1000 mm/s, depending on the wave's speed, with an accuracy of ±2 mm/s. The whole setup is shown in figure 2.15. Again a paddle was used to generate one solitary wave per measurement. Since the linear motor was already in use to move the slide with the camera and the laser, the paddle was now driven by a step motor from *NanoTech* for the streamline measurements. After the wave was released by the paddle, the linear motor started moving the slide with the camera and the laser, as soon as the wave approached the recording area. Once the slide had reached its target velocity which was the wave's speed v_s, the wave was exactly in front of the camera and the shutter of the camera was opened for an exposure time of $1/21$ s. The wave's velocity v_s was considered as constant for this short period of time. Hence, the scattering particles that moved relative to the moving coordinate system were visualized as streamlines by the camera.

31
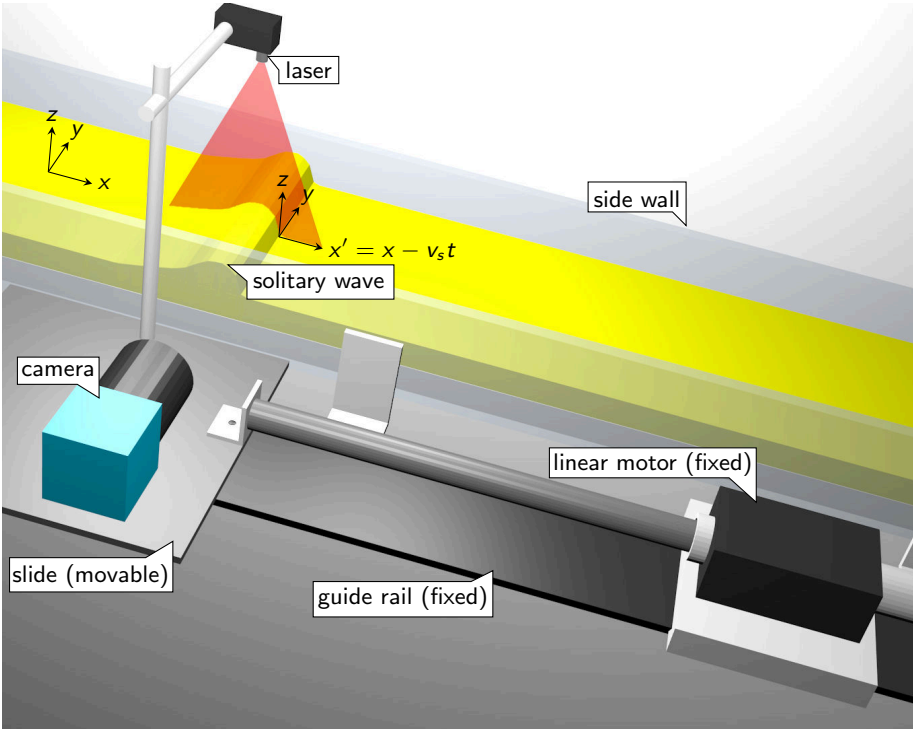
Figure 2.15: Experimental setup for the measurement of the streamlines: The guide rail was fastened parallel to the channel and hence parallel to the x-axis of the laboratory coordinate system. The laser and camera were mounted on the slide which was dragged along the guide rail by the linear motor with the wave's velocity v_s. Thus, the streamlines were recorded relative to the wave's speed. Reproduced with permission form [98]. ©2015, AIP Publishing LLC.

2.2.3 Dimensionless quantities

For the reasons that were described in section 2.1.4, the characteristic quantities for the wave dynamics were made dimensionless by using the Nusselt free surface velocity u_s and film thickness d_n, irrespective of the kind of topography (figure 2.2) that was used for a certain experiment. For the continuous waves, the shape of the waves h_c, the amplitude a_c and the wave number k_c were normalized by the Nusselt film thickness d_n and the phase velocity v_c by the Nusselt free surface velocity u_s:

$$h_c^* = \frac{h_c}{d_n}, \tag{2.16}$$

$$a_c^* = \frac{a_c}{d_n}, \tag{2.17}$$

$$k_c^* = k_c \cdot 2\pi d_n, \tag{2.18}$$

$$v_c^* = \frac{v_c}{u_s}. \tag{2.19}$$

For the solitary waves, the shape of the waves h_s, the amplitude a_s and the full length at half maximum λ_s were normalized by the Nusselt film thickness d_n and the phase velocity v_s by the Nusselt free surface velocity u_s:

$$h_s^* = \frac{h_s}{d_n}, \tag{2.20}$$

$$a_s^* = \frac{a_s}{d_n}, \tag{2.21}$$

$$\lambda_s^* = \frac{\lambda_s}{d_n}, \tag{2.22}$$

$$v_s^* = \frac{v_s}{u_s}. \tag{2.23}$$

3 Theoretical description of the viscous film flow

As already mentioned, the Navier-Stokes equations cannot be solved exactly for film flows over strongly undulated substrates. Because of that, the following mathematical derivations for the film flow problem are restricted to flat substrates.

3.1 Steady state solution

By solving the Navier-Stokes equations, the velocity field $\vec{u}^* = \vec{u}/u_s$ and the pressure distribution $p^* = p/\left(\rho u_s{}^2\right)$ of the basic film flow over the flat substrate are derived in dimensionless form (details shown in e.g. [96]). The dimensionless lengths are defined by $x^* = x/d_n$ and $z^* = z/d_n$, the dimensionless time by $t^* = tu_s/d_n$. It is assumed that the velocity field of the steady gravity-driven film flow is unidirectional in x^*-direction and that its magnitude only depends on the z^*-coordinate (figure 3.1): $\vec{u}^* = (U^*(z^*), 0, 0)$. The continuity equation is then fulfilled identically.
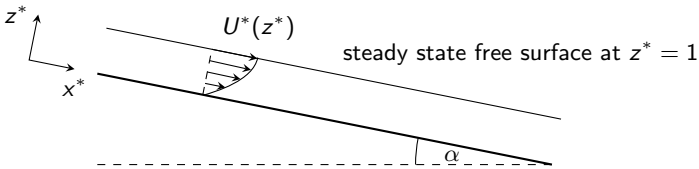

Figure 3.1: A sketch of the dimensionless description of a steady gravity-driven film flow. The velocity field is unidirectional in x^*-direction and does only depend on the z^*-coordinate. The free surface has the curvature zero and is located at $z^* = 1$.

The x- and z-component of the Navier-Stokes equations combined with equations 2.2, 2.3 and 2.6 yield:

$$x: \quad 0 = -\frac{\partial P^*}{\partial x^*} + \frac{1}{Re}\left(2 + \frac{\partial^2 U^*}{\partial z^{*2}}\right) \tag{3.1}$$

$$z: \quad 0 = -\frac{\partial P^*}{\partial z^*} - \frac{2}{Re\tan\alpha}. \tag{3.2}$$

P^* is the pressure distribution of the basic flow. The boundary condition at the substrate is the no-slip condition. At the free surface, the tangential stress is zero and the normal stress is equal to the pressure in the gas phase above which is constant and can be chosen arbitrarily:

$$U^*\left(z^* = 0\right) = 0; \qquad \left.\frac{\partial U^*}{\partial z^*}\right|_{z^*=1} = 0; \qquad P^*\left(z^* = 1\right) = const = 0. \tag{3.3}$$

That leads to the solution for the velocity field $\vec{u}^* = (U^*, 0, 0)$ and pressure distribution P^* of the basic flow:

$$U^* = -z^{*2} + 2z^* \tag{3.4}$$

$$P^* = \frac{2}{Re\tan\alpha}\left(1 - z^*\right). \tag{3.5}$$

If waves appear on a gravity-driven film flow, the assumptions made in this section are not valid anymore and hence one has to return to the original Navier-Stokes equations. Without any simplifying assumptions, an exact analytical solution of these is impossible (in fact, the proof, if the Navier-Stokes equations have a solution, is one of the "Millennium-problems" posed by the "Clay Mathematics Institute" in 2000 [99]). To reduce the complexity of the equations, numerous models for the wave evolution were formulated and will be described in the following sections 3.2 and 3.3.

3.2 Linear continuous waves and the Orr-Sommerfeld equation

The Orr-Sommerfeld equation was first derived by William McFadden Orr [47] and Arnold Sommerfeld [45, 46]. It was developed to decide, if an arbitrary flow

is stable or unstable against infinitesimally small disturbances. Solving it also returns the grade of this stability and the phase velocity of the emerging waves. Several authors adapted the equation for film flows over flat substrates with a free surface, e.g. Lin [65], Benjamin [44] or Yih [43]. Since the results obtained by solving the Orr-Sommerfeld equation will be compared to the experimental data, its derivation from the Navier-Stokes equations as well as its numerical solution is described below and follows in large parts [43] and [75], pages 11 ff. This dissertation deals with the two-dimensional problem and hence omits the y-component of the flow.
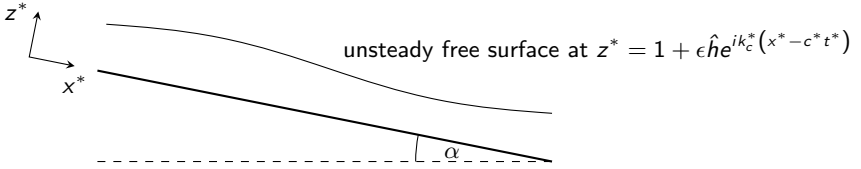

Figure 3.2: A sketch of the dimensionless description of the unsteady film flow. Due to the perturbations, the curvature of the free surface is not zero and has to be taken into account for the formulation of the boundary conditions.

In order to test the stability of this flow against small disturbances, infinitesimal sinusoidal perturbations are added to the steady state solutions of the dimensionless Navier-Stokes equations 3.4 and 3.5 and to the free surface shape (figure 3.2):

$$u^*(x^*, z^*, t^*) = U^*(z^*) + \epsilon \hat{u}(z^*) e^{ik_c^*(x^* - c^* t^*)} \tag{3.6}$$

$$w^*(x^*, z^*, t^*) = \epsilon \hat{w}(z^*) e^{ik_c^*(x^* - c^* t^*)} \tag{3.7}$$

$$p^*(x^*, z^*, t^*) = P^*(z^*) + \epsilon \hat{p}(z^*) e^{ik_c^*(x^* - c^* t^*)} \tag{3.8}$$

$$h_c^*(x^*, t^*) = 1 + \epsilon \hat{h} e^{ik_c^*(x^* - c^* t^*)}. \tag{3.9}$$

Equations 3.6 through 3.8 are substituted into the original dimensionless Navier-Stokes equations and the continuity equation. The perturbation factor is taken to the limit $\epsilon \to 0$ for the linearized problem. That means, all terms propor-

tional to ϵ will be omitted in the following:

$$ik_c^*\hat{u}(U^* - c^*) + \hat{w}\frac{\partial U^*}{\partial z^*} + ik_c^*\hat{p} = \frac{1}{Re}\left(\frac{\partial^2\hat{u}}{\partial z^{*2}} - k_c^{*2}\hat{u}\right) \quad (3.10)$$

$$ik_c^*\hat{w}(U^* - c^*) + \frac{\partial\hat{p}}{\partial z^*} = \frac{1}{Re}\left(\frac{\partial^2\hat{w}}{\partial z^{*2}} - k_c^{*2}\hat{w}\right) \quad (3.11)$$

$$ik_c^*\hat{u} + \frac{\partial\hat{w}}{\partial z^*} = 0. \quad (3.12)$$

After introduction of the stream function

$$\frac{\partial\psi}{\partial z^*} := \hat{u} \quad (3.13)$$

$$-\frac{\partial\psi}{\partial x^*} := \hat{w}, \quad (3.14)$$

eliminating $\hat{p}$ and all x^*-derivatives leads to the Orr-Sommerfeld equation:

$$\frac{\partial^4\psi}{\partial z^{*4}} - 2k_c^{*2}\frac{\partial^2\psi}{\partial z^{*2}} + k_c^{*4}\psi = ik_c^* Re\left[(U^* - c^*)\left(\frac{\partial^2\psi}{\partial z^{*2}} - k_c^{*2}\psi\right) - \psi\frac{\partial^2 U^*}{\partial z^{*2}}\right].$$
$$(3.15)$$

The displacement of the free surface $\hat{h}$ has to be calculated from the kinematic boundary condition at the free surface:

$$\vec{n}\cdot\vec{u}^* = \frac{\partial h_c^*}{\partial t^*} \quad (3.16)$$

$$\hat{h} = \frac{\hat{w}(z^* = 1)}{ik_c^*(U^* - c^*)} = -\frac{\psi(z^* = 1)}{U^* - c^*}, \quad (3.17)$$

with $\vec{n}(x^*, t^*)$ being the vector normal to the unsteady free surface. The boundary condition at $z^* = 0$ is still the no slip condition $u^* = w^* = 0$ which combined with 3.12 through 3.14 results in:

$$\left.\frac{\partial\psi}{\partial z^*}\right|_{z^*=0} = 0 \quad (3.18)$$

$$\psi(z^* = 0) = 0. \quad (3.19)$$

At the free surface, the tangential stress still has to be zero ($\vec{m}(x^*, t^*)$: vector tangential to the free surface; $\vec{t}(x^*, t^*)$: stress vector, dimensionless)

$$\vec{m}\cdot\vec{t} = 0, \quad (3.20)$$

but the normal stress now exhibits a jump because it has to balance out the normal stress induced by the surface tension of the curved free surface (Young-Laplace equation):

$$\vec{n} \cdot \vec{t} = \kappa^* Ka \left(\frac{2}{Re^5 \sin \alpha} \right)^{1/3} . \tag{3.21}$$

The stress vector $\vec{t}$ is calculated from equations 3.6 and 3.7. The curvature $\kappa^*(x^*, t^*)$ and the vectors normal $\vec{n}$ and tangential $\vec{m}$ to the free surface are calculated from equation 3.9. Then equations 3.17, 3.20 and 3.21 lead to the following relations at $z^* = 1$:

$$0 = -\frac{\hat{w}}{ik_c^*} \left(\frac{2}{1 - c^*} + k_c^{*2} \right) + \frac{\partial \hat{u}}{\partial z^*} \tag{3.22}$$

$$\hat{p} = \frac{1}{Re} \left[2 \frac{\partial \hat{w}}{\partial z^*} + \hat{h} \left(\frac{2}{\tan \alpha} + Ka k_c^{*2} \left(\frac{2}{Re^2 \sin \alpha} \right)^{1/3} \right) \right] . \tag{3.23}$$

The pressure is removed by using equation 3.10 and equation 3.5 at $z^* = h_c^*$; $\hat{w}$ and its derivative by using equation 3.12. The stream function (equations 3.13 and 3.14) is again put in place and so the boundary conditions for the Orr-Sommerfeld equation 3.15 at the free surface $z^* = 1$ are:

$$\left(k_c^{*2} + \frac{2}{1 - c^*} \right) \psi + \frac{\partial^2 \psi}{\partial z^{*2}} = 0 \tag{3.24}$$

$$\frac{\partial^3 \psi}{\partial z^{*3}} + \frac{\partial \psi}{\partial z^*} \left[-3k_c^{*2} - ik_c^* Re(1 - c^*) \right] =$$

$$= -ik_c^* \frac{\psi}{1 - c^*} \left[\frac{2}{\tan \alpha} + k_c^{*2} Ka \left(\frac{2}{Re^2 \sin \alpha} \right)^{1/3} \right] . \tag{3.25}$$

The Orr-Sommerfeld equation (equation 3.15) and its boundary conditions (equations 3.18, 3.19, 3.24 and 3.25) constitute an eigenvalue problem. The complex wave velocity c^* is said eigenvalue and depends on Re, k_c^*, α and Ka. The real part $\mathcal{R}(c^*)$ is the phase velocity v_c^* of the linear continuous waves and the imaginary part multiplied with the wave number is their exponential growth rate $b^* = \mathcal{I}(c^*) \times k_c^*$. When $b^* > 0$, the waves grow, otherwise they are damped on their way downstream.

This eigenvalue problem cannot be solved exactly for the whole parameter space. It is possible to solve it for infinitely long waves with $k_c^* = 0$ (0th approximation). The Orr-Sommerfeld equation and its boundary conditions then become:

$$\frac{\partial^4 \psi}{\partial z^{*4}} = 0; \tag{3.26}$$

$$z^* = 0: \quad \frac{\partial \psi}{\partial z^*} = 0; \quad \psi = 0; \tag{3.27}$$

$$z^* = 1: \quad \frac{2}{1 - c^*}\psi + \frac{\partial^2 \psi}{\partial z^{*2}} = 0; \quad \frac{\partial^3 \psi}{\partial z^{*3}} = 0. \tag{3.28}$$

Integrating equation 3.26 four times and using the boundary conditions leads only then to a nontrivial solution, if the eigenvalue

$$c^* = 2. \tag{3.29}$$

That means that the phase velocity of infinitely long waves $v_c(k_c^* = 0) = \mathcal{R}(c^*) \times u_s = 2 \times u_s$ is twice as high as the Nusselt free surface velocity. Their growth rate $b^*(k_c^* = 0) = 0$. The eigenfunction is then

$$\psi(k_c^* = 0) = z^{*2}. \tag{3.30}$$

For long waves with $k_c^* \to 0$ (1st approximation), the terms of the Orr-Sommerfeld equation (equation 3.15) and the boundary conditions (equations 3.18, 3.19, 3.24, 3.25) proportional to k_c^{*2} are set to zero. An exception is the term that contains the Kapitza number in equation 3.25. High Kapitza numbers make the term that contains them non-negligible, irrespective of the wave number. Then the solution of the 0th approximation is substituted into the Orr-Sommerfeld equation and its boundary conditions. The resulting eigenvalue is

$$c^* = 2 + i \left(\frac{4k_c^* Re}{5} - k_c^* \left(\frac{1}{\tan \alpha} + \frac{k_c^{*2} Ka}{2} \left(\frac{2}{Re^2 \sin \alpha} \right)^{1/3} \right) \right). \tag{3.31}$$

The neutral curve is located where the imaginary part of the eigenvalue $\mathcal{I}(c^*) = 0$. This leads to the critical Reynolds number for $k_c^* \to 0$:

$$Re_c = \frac{5}{4 \tan \alpha}. \tag{3.32}$$

The eigenvalue and eigenfunction for $k_c^* = 0$ can be taken as a starting point for an iterative numerical procedure to calculate c^* for higher wave numbers by increasing k_c^* gradually. A numerical shooting method was used, where the eigenfunction and -value of the next smaller wave number were taken as the initial guesses for the eigenvalue and the initial condition of $\partial^3 \psi / \partial z^{*3}$ at $z^* = 0$. The new eigenfunction and eigenvalue were calculated numerically with a Runge-Kutta-procedure (see e.g. [100] page 20 ff.) and the deviation from the boundary conditions at $z^* = 1$ were determined. With the help of a Newton-Raphson-approach (see e.g. [101] page 7 ff.), these deviations were reduced until they were below 10^{-6} (convergence criterion) and eventually, the eigenfunction and the eigenvalue c^* for the new wave number were retrieved. The resulting growth rates for three different Reynolds numbers, the Kapitza number $Ka = 2.01$ and inclination angle $\alpha = 10°$ are plotted on the left hand side of figure 3.3. When the growth rate is negative, the film flow is steady, otherwise, waves appear at the free surface. By calculating the wave number k_c^*, where the growth rate $b^* = 0$ for all Reynolds numbers, one receives the stability map $(k_c^*(Re)$, where $b^* = 0$) on the right hand side of figure 3.3.
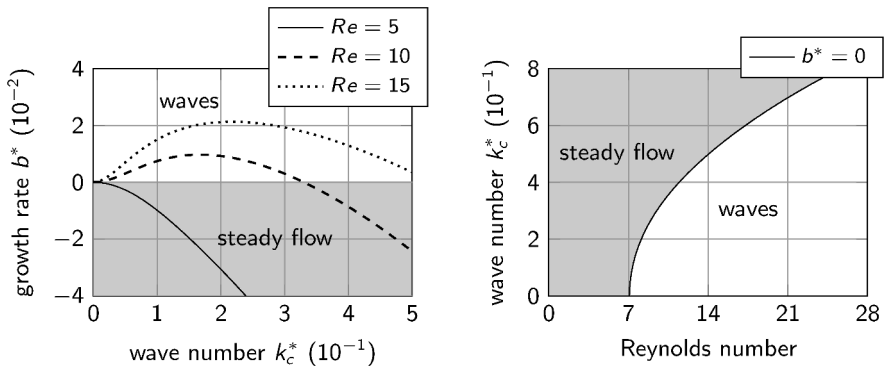

Figure 3.3: Left: The growth rates obtained by solving the Orr-Sommerfeld equation numerically with $Ka = 2.01$ and $\alpha = 10°$. The Reynolds numbers were set to three different values; one below and two above the critical Reynolds number $Re_c = 7.1$. The growth rate $b^* = \mathcal{I}(c^*) \times k_c^*$. **Right:** The stability map $k_c^*(Re)$, where $b^* = 0$.

3.3 Model equations for nonlinear wave dynamics

There are several excellent reviews about the different model equations for the wave evolution on gravity-driven film flows, most notably by Craster and Matar [90], Chang [89], Kalliadasis et al. [102] and Chang and Demekhin [75]. Thus, only a quick overview of the most prominent examples is given in this section.

The **Benney equation** (derived e.g. in [67, 68, 75, 103]) is an example for a long-wave approximation of the Navier-Stokes equations. As for the Orr-Sommerfeld equation, non-steady waves are added to the steady state solution of equations 3.4 and 3.5 and inserted into the original Navier-Stokes equations and its boundary conditions. Instead of setting the amplitude of these disturbances to zero, the dimensionless wave number is regarded as small, $k_c^* \ll 1$ and hence all parameters proportional to k_c^{*2} are set to zero. Also, since k_c^* is small, all derivatives in the stream wise direction x^* are also small and thus of order $O(k_c^*)$. Using a stream function (equations 3.13 and 3.14) and a power series expansion then yields the Benney equation for the evolution of the free surface contour $h_c^*(x^*, t^*)$:

$$\frac{\partial h_c^*}{\partial t^*} + \frac{\partial}{\partial x^*}\left(\frac{2}{3}h_c^{*3} + k_c^*\left(\frac{8}{15}Reh_c^{*6} - \frac{2}{3}\frac{h_c^{*3}}{\tan\alpha}\right)\frac{\partial h_c^*}{\partial x^*}\right) = 0. \qquad (3.33)$$

For the long wave expansion described above, one has to assume a priori that the Weber number $We = 2^{1/3} \times Ka \times Re^{-5/3} \times \sin^{-1/3}\alpha$ is of order $O(k_c^{-2})$ (see e.g. [68]). Accordingly, the term in the Benney equation proportional to $We \times k_c^{*2}$ cannot be neglected and the Benney equation has to be complemented by a surface tension term (marked purple):

$$\frac{\partial h_c^*}{\partial t^*} + \frac{\partial}{\partial x^*}\left(\frac{2}{3}h_c^{*3} + k_c^*\left(\frac{8}{15}Reh_c^{*6} - \frac{2}{3}\frac{h_c^{*3}}{\tan\alpha}\right)\frac{\partial h_c^*}{\partial x^*} + \frac{2}{3}k_c^{*3}Weh_c^{*3}\frac{\partial^3 h_c^*}{\partial x^{*3}}\right) = 0. \qquad (3.34)$$

The Benney equation can be linearized (see e.g. [74, 102, 104]) analogously to the linearization of the Navier-Stokes equations by using the ansatz from equation 3.9 for equation 3.34. After neglecting all terms proportional to ϵ and setting the imaginary part of the complex phase velocity to zero, one obtains

the neutral curve in the stability map (wave number - Reynolds number plane):

$$k_c^* = \sqrt{\frac{4Re - 5\cot\alpha}{5We}}. \tag{3.35}$$

From this equation, it can easily be seen that for $k_c^* = 0$ the same critical wave number is obtained as by the Orr-Sommerfeld equation (equation 3.32). Here it has to be mentioned that equation 3.35 is only valid for $Re - Re_c$ of order $O(k_c^{*2})$. Pumir et al. [105] revealed that the solution of the Benney equation blows up for moderate or high Reynolds numbers, i.e the amplitude of the waves grows without saturation and no bounded solutions are obtained. According to these findings, Oron and Gottlieb [104] divided the stability map of the Benney equation into three regions: The linearly stable region (i), the linearly unstable region where the waves reach saturation (ii), and the linearly unstable region where the waves do not reach saturation (iii). Regions (i) and (ii) are separated by equation 3.35 and regions (ii) and (iii) by a numerically obtained boundary. They also found that the bifurcation type changes when going from the first-order Benney equation to second-order. This presents an evidence of a poor convergence of the asymptotic procedure resulting in the Benney equation. Takeshi [106] approached the problem of the unbounded solutions by using a Padé-approximation and extended the validity of the Benney equation to higher Reynolds numbers.

The **boundary layer** approach for the wave dynamics again uses $k_c^* \ll 1$, see e.g. [75, 89]. Furthermore, the magnitude of the Weber number is a priori defined as: $We \times Re \times k_c^{*-3} = O(1)$. That means that for Reynolds numbers of order $O(10)$, the Kapitza number must be of Order $O(10^3)$ to fulfill $k_c^* \ll 1$. For a vertical wall ($\alpha = 90\,^\circ$), the Navier-Stokes equations, the continuity equation and their boundary conditions become (from [75]):

$$\frac{\partial u^*}{\partial t^*} + u^*\frac{\partial u^*}{\partial x^*} + w^*\frac{\partial u^*}{\partial z^*} = \frac{9Ka^{1/3}}{(2Re)^{11/9}}\left(\frac{\partial^3 h_c^*}{\partial x^{*3}} + \frac{1}{3}\frac{\partial^2 u^*}{\partial x^{*2}} + 1\right), \tag{3.36}$$

$$\frac{\partial u^*}{\partial x^*} + \frac{\partial w^*}{\partial z^*} = 0, \tag{3.37}$$

$$z^* = h_c^*(x^*, t^*): \quad w^* = \frac{\partial h_c^*}{\partial t^*} + u^*\frac{\partial h_c^*}{\partial x^*}, \quad \frac{\partial u^*}{\partial z^*} = 0, \tag{3.38}$$

$$z^* = 0: \quad u^* = w^* = 0. \tag{3.39}$$

In order to further simplify these equations, a procedure from the original boundary layer theory (see e.g. in [96]) was adapted for gravity-driven film flows. There, boundary layers are calculated approximately by using "methods, where the equation of motion are not satisfied everywhere in the field but only in integral means across the boundary layer" ([96] p. 440). Shkadov [107] carried this out by assuming an ad hoc velocity profile for the dependence of u^* from the z^*-coordinate, e.g. a self-similar parabolic equation. This is then called an **integral boundary layer (IBL)** model equation. Improvements on this matter were achieved by using weighted residuals on the integral boundary layer equation **(WRIBL)**, as shown e.g. by Ruyer-Quil and Manneville [72], Scheid et al. [94] and Oron and Heining [108].

Both the Benney equation and the boundary layer approach are long-wave approximations, thus $k_c^* \ll 1$. Furthermore, the Weber number has to be of order $O(k_c^{*2})$. These requirements are not met in the experiments presented in this manuscript, so the nonlinear model equations described here are not applicable to the results shown in the following chapter 4.

4 Results and discussion

4.1 Continuous wave dynamics

As mentioned in section 1.3, the dynamics of free surface waves over undulated inclines has been studied only scarcely in the literature. The experiments carried out and described in this section aim to reveal the influence of different corrugation shapes (figure 2.2) on the evolution of these waves.

4.1.1 Measured parameter space

In order to scrutinize the influence of the four different substrate topographies (figure 2.2) S_0 (flat), S_1 (sinusoidal), S_2 (saw-tooth-like) and S_3 (rectangular) on the dynamics of continuous waves, the respective results were gathered for a film flow of the oil *Elbesil 100* (parameters in table 2.1) at the measurement temperature

$$\theta = (23.0 \pm 0.2) \, ^\circ\mathrm{C} \tag{4.1}$$

and the inclination angle

$$\alpha = (10.0 \pm 0.1) \, ^\circ. \tag{4.2}$$

The volume flux $\dot{V}$ of the basic flow was set to a constant value of

$$\dot{V} = (140 \pm 3) \, \frac{\mathrm{cm}^3}{\mathrm{s}}. \tag{4.3}$$

The corresponding Nusselt film thickness d_n, Nusselt free surface velocity u_s and Reynolds number Re can then be calculated from equations 2.2, 2.3 and

2.5, respectively:

$$d_n = (5.3 \pm 0.1)\,\text{mm}, \tag{4.4}$$

$$u_s = (232 \pm 6)\,\frac{\text{mm}}{\text{s}}, \tag{4.5}$$

$$Re = 11.9 \pm 0.5\,. \tag{4.6}$$

The substrate topography S_0 was used as a reference, since the wave dynamics on flat substrates has been studied extensively in the literature, e.g. [70, 71, 75, 77, 79–81, 89, 90, 107].

In the linear regime, the growth rates and phase velocities of sinusoidal free surface waves can be calculated numerically from the Orr-Sommerfeld-equation (section 3.2). In order to validate the experiments, these results will be compared to the measurements of the dynamics of sinusoidal waves with a very small amplitude over the flat substrate. Then the wave dynamics were measured for film flows over the other three substrates S_1, S_2 and S_3. Also nonlinear waves with much larger amplitudes were scrutinized experimentally.

4.1.2 The wave evolution in the linear regime

The evolution of the waves in the linear regime was investigated by exciting waves with a very small amplitude at the inlet of the channel. The paddle's amplitude was set to

$$a_{p,0} = 0.25\,\text{mm} \tag{4.7}$$

and the paddle's frequency was set to seven different values,

$$f_p = \{1.0, 1.5, 2.0, 2.5, 3.0, 4.0, 5.0\}\,\text{Hz}. \tag{4.8}$$

The resulting wave's propagation down the channel was recorded with the setup described in section 2.2.

As an example, the result for the flat substrate S_0 with the paddle's frequency $f_p = 3.0\,\text{Hz}$ is shown in figure 4.1 at five different times. The graph reveals that the initially sinusoidal waves travel downstream, grow and change their shape on their way down the channel. Since these data were to be compared to

the calculations from the Orr-Sommerfeld equation (section 3.2), the measured waves had to meet the criteria of linear, harmonic disturbances (equations 3.6 through 3.9). That means that waves were considered as linear, if the ratio of the wave's amplitude to Nusselt film thickness $a_c^* = a_c/d_n$ was smaller than 0.04 and if the waves showed a sinusoidal profile.
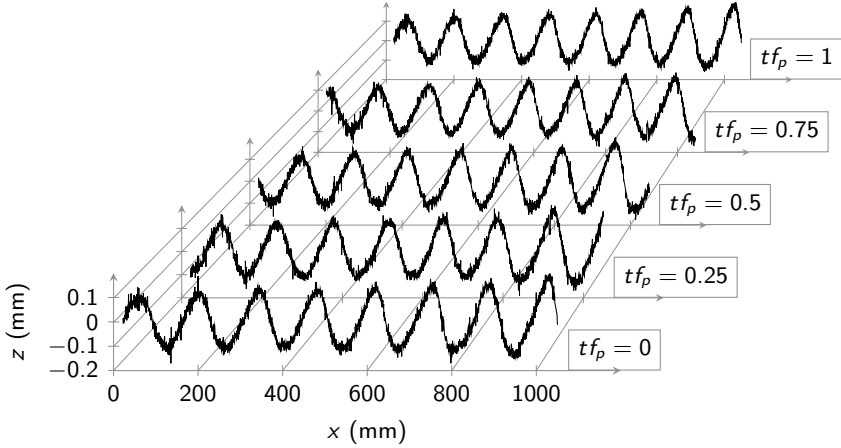

Figure 4.1: The evolution of continuous waves $h_c(x, t)$ over the flat substrate S_0; $a_{p,0} = 0.25\,\mathrm{mm}$, $f_p = 3.0\,\mathrm{Hz}$, $Re = 11.9$, $Ka = 2.01$.

The solution of the Orr-Sommerfeld equation yields the wave's phase velocity v_c^* and exponential growth rate b^* in relation to the wave number k_c^*. These three quantities were extracted from the measurements by fitting the function

$$h_c^*(x^*, t^*) = a e^{b^* v_c^{*-1} \cdot x^*} \sin\left(k_c^*(x^* - phase(t^*))\right) \tag{4.9}$$

which was suggested by Liu et al. [48], to the shape of the waves that met the criteria for linear waves at all 1200 recorded time steps . Figure 4.2 shows the waves for all seven measured frequencies at one random time in dimensionless representation. Since not all waves in figure 4.2 meet the conditions for linearity for the whole channel, the fitting procedure was restricted to a section shorter than the channel's length for most paddle frequencies.

In the linear regime, the parameters k_c^*, b^* and v_c^* have to be considered as constant. The phase velocity v_c^* and its error were calculated from $phase(t^*)$ with the help of linear regression. The other fit parameters k_c^* and $b^* v_c^{*-1}$ were averaged over the 1200 time steps. The respective errors were estimated by computing the standard deviation over the same time frame.
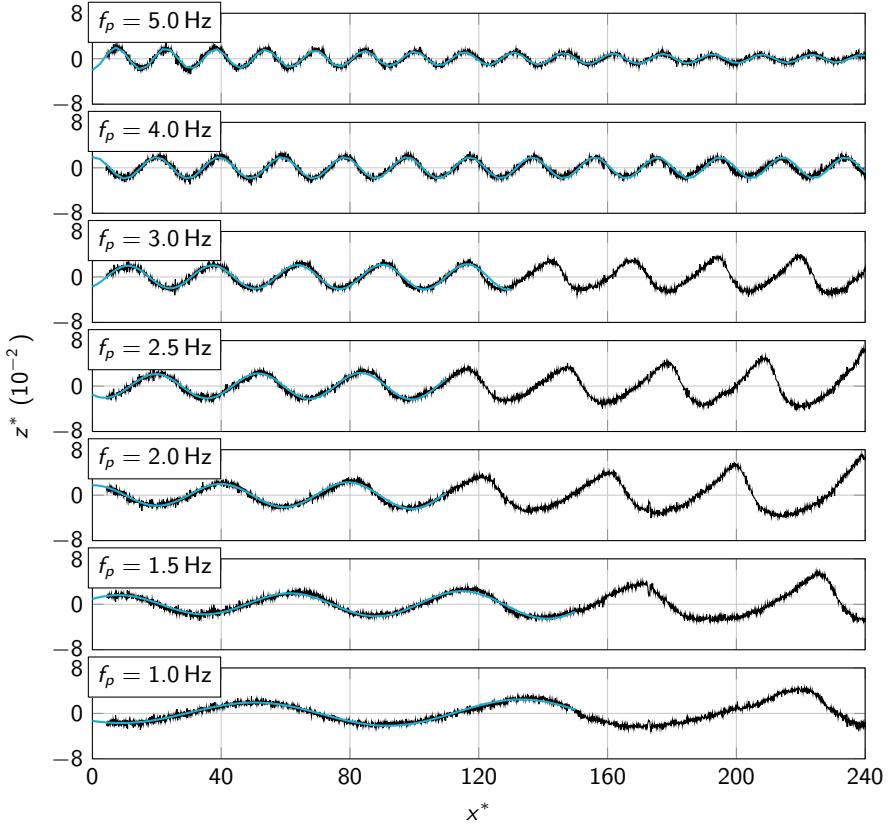

Figure 4.2: The wave's shape $h_c^*(x^*, t^*)$ (black lines) at a random time for S_0, $Ka = 2.01$, $Re = 11.9$, $a_{p,0} = 0.25\,\text{mm}$ and all seven paddle frequencies. The fit (cyan lines) from equation 4.9 was used for the sections of the waves which met the linear criteria.

In figure 4.3 the experimental results are compared to the numerical ones. Concerning the growth rates, the two curves are qualitatively very similar, but differ from each other quantitatively. The reason for that is the finite amplitude of the waves in the experiments, while in the numerical calculations, the amplitude of the disturbances ϵ was infinitesimally small. The wave number, where the growth rate is numerically calculated as zero is defined as the critical wave number. Especially the values near the critical wave number are very sensitive and show a big gap between the numerical and experimental data. The fact that the experimental growth rates are consistently smaller than the numerical ones indicates that the growth rates depend strongly on the amplitude of the waves. Comparing the phase velocities in figure 4.3 exhibits very similar numerical and experimental curves. Overall, the validation of the experiments is successful, considering the finite wave amplitudes in the experiments.
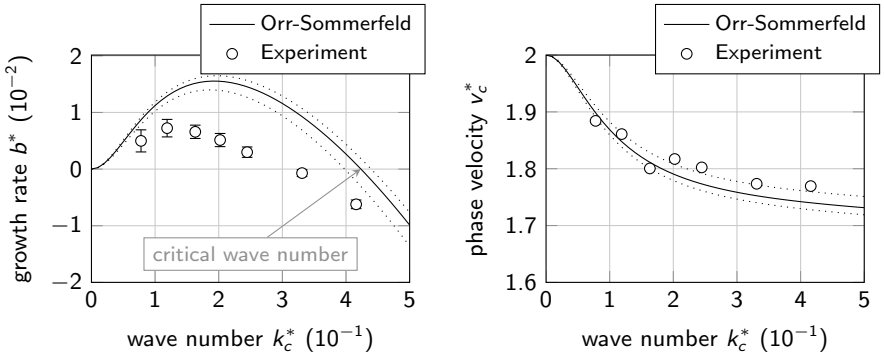

Figure 4.3: Comparison between the results obtained by solving the Orr-Sommerfeld equation 3.15 (solid line: $Re = 11.9$, dotted lines: $Re = 11.9 \pm 0.5$, see equation 4.6) and the ones from the experiments carried out over the flat substrate S_0. The dimensionless wave number k_c^*, growth rate b^* and phase velocity v_c^* are provided by averaging the fitting parameters of equation 4.9 over 1200 time steps. The errors were calculated from the standard deviations and are smaller than the symbols for k_c^* and v_c^*.

The graphs in figure 4.4 demonstrate the evolution of the waves, generated with the same paddle amplitude and frequency as in figure 4.1, but over the sinusoidal substrate S_1. When these are compared to the waves over the flat substrate S_0 (figure 4.1), some differences are obvious: As aforementioned in section 2.1.5, the basic flow over the sinusoidal substrate S_1 exhibits steady waves due to the undulation of the substrate. That leads to the dependence of the unsteady wave's amplitude on the position inside a substrate's wavelength. This is visible in figure 4.4 by the short dents that do not move and overlay the longer unsteady waves. Also the unsteady waves grow much faster than the ones that run over the flat substrate and consequently fulfill the linear criteria for a much shorter section of the channel.
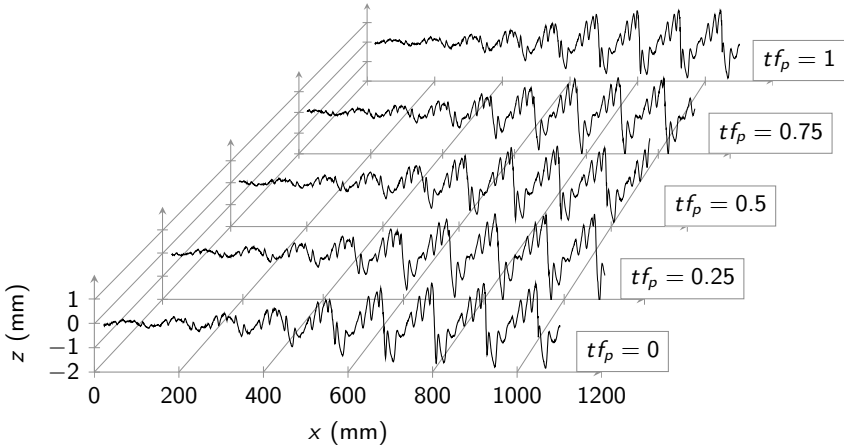

Figure 4.4: The evolution of continuous waves $h_c(x, t)$ over the sinusoidal substrate S_1; $a_{p,0} = 0.25\,\text{mm}$, $f_p = 3.0\,\text{Hz}$, $Re = 11.9$, $Ka = 2.01$.

Despite the forecited dents, it was still possible to fit the function in equation 4.9 to the measured shapes of the waves. Due to the short distance, where the linear criteria were met for most paddle frequencies, the fit could only be made over little more than one wavelength of the unsteady wave, as exhibited in figure 4.5. Hence, the fit parameters were error prone, but this error could be reduced by averaging over the 1200 time steps. The error was estimated

by again computing the standard deviation. Similar results were obtained by the measurements over the other undulated topographies S_2 and S_3. These are shown in figure 4.6 exemplarily for the frequency $f_p = 3.0\,\text{Hz}$, again with equation 4.9 fitted to the experimental data in the linear regime.
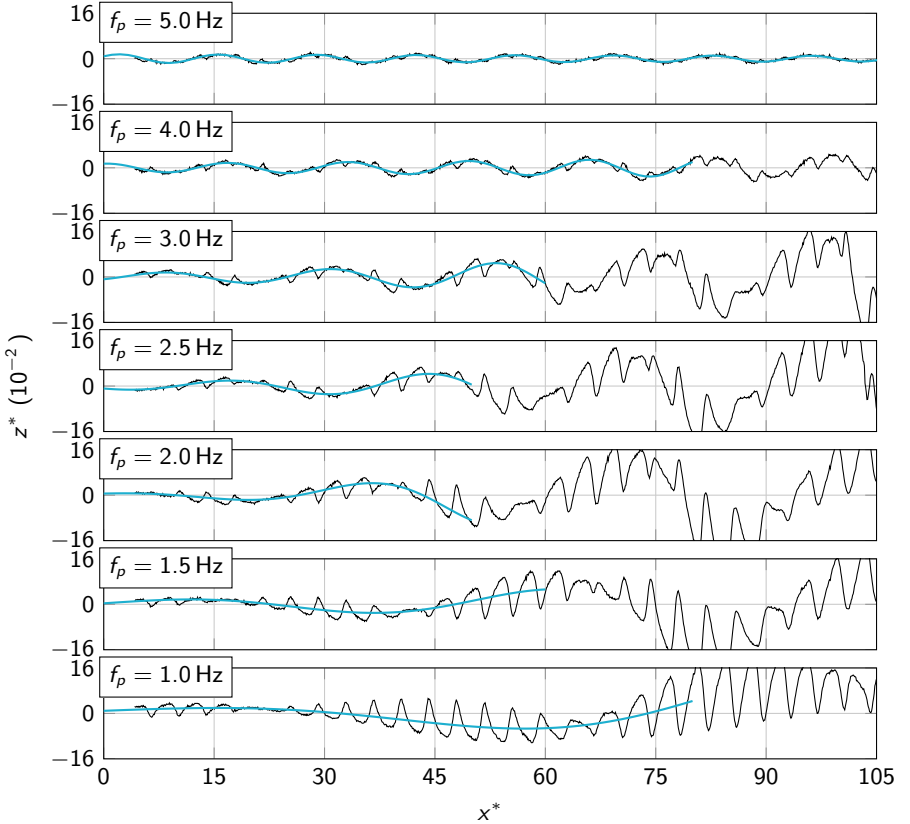

Figure 4.5: The wave's shape $h_c^*(x^*, t^*)$ (black lines) at a random time for S_1, $Ka = 2.01$, $Re = 11.9$, $a_{p,0} = 0.25\,\text{mm}$ and all seven paddle frequencies. The fit (cyan lines) from equation 4.9 was used for the sections of the waves which met the linear criteria.

Figure 4.7 compares the growth rates and phase velocities in the linear regime for the flows over all four substrates $S_0 - S_3$. The much faster growth of the linear waves flowing over an undulated substrate compared to the flat substrate is confirmed. The flow is strongly destabilized by the substrate's undulations for the measured Reynolds number $Re = 11.9$. The differences between S_1, S_2 and S_3 are much smaller, but still noticeable. Qualitatively, the curves of the growth rates do not differ from each other. They have a maximum near a wave number $k_c^* \approx 0.15$ and go to zero at $k_c^* \approx 0.4$. For infinitely long waves ($k_c^* = 0$), the growth rate tends towards zero not only for the flat, but also for the undulated substrates. Recent measurements of Schörner et al. [63] look further into the destabilizing effects of substrate undulations.

The waves over the undulated substrates travel significantly slower than the ones over the flat substrate. Here also, the differences between the results for the undulated topographies are much smaller than between an undulated and the flat substrate.
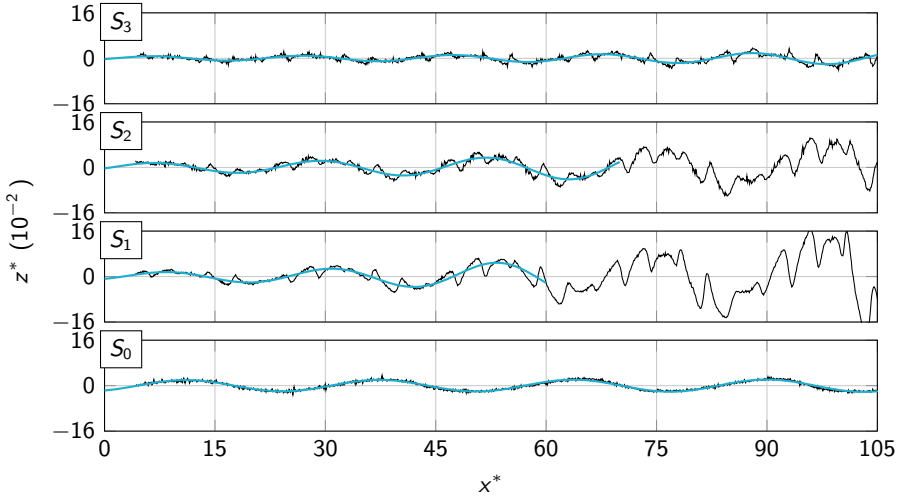

Figure 4.6: The wave's shape $h_c^*(x^*, t^*)$ (black lines) at a random time for $f_p = 3.0\,\mathrm{Hz}$, $Ka = 2.01$, $Re = 11.9$, $a_{p,0} = 0.25\,\mathrm{mm}$ and all four substrates. The fit (cyan lines) from equation 4.9 was used for the sections of the waves that met the linear criteria.
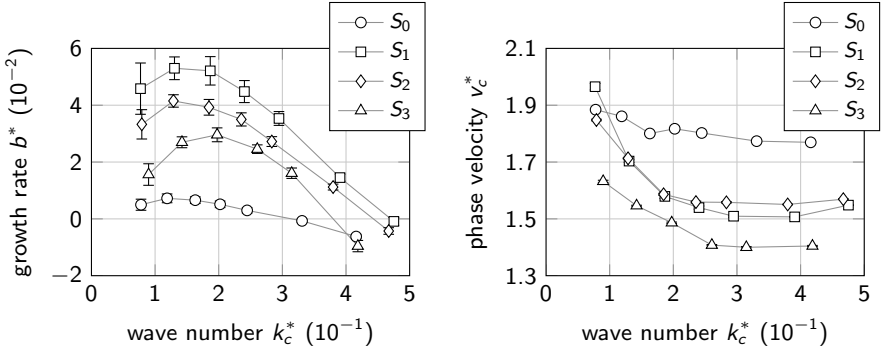
Figure 4.7: Comparison of the growth rates (left) and phase velocities (right) of linear free surface waves over different substrates with $Re = 11.9$. The dimensionless wave number k_c^*, growth rate b^* and phase velocity v_c^* are provided by averaging the fitting parameters of equation 4.9 over time. The respective errors were calculated from the standard deviations and are smaller than the symbols for k_c^* and v_c^*.

4.1.3 The wave evolution in the nonlinear regime

Once the waves, which were excited by the paddle at the channel's inlet, do no longer meet the linear criteria from section 4.1.2, it is not possible to use equation 4.9 anymore. Also comparisons to the solutions provided by the Orr-Sommerfeld equation are no longer adequate. The nonlinear models described in section 3.3 fail for this parameter space, too. The evolution of the waves under different circumstances could nevertheless be measured experimentally. Since the requirement for very small wave amplitudes is not present for nonlinear waves, it was possible to use different paddle amplitudes

$$a_{p,0} = \{0.25, 1.0, 4.0\} \text{ mm}, \tag{4.10}$$

still at the same frequencies as in equation 4.8. Thus, waves of different initial amplitudes and the same frequencies as in section 4.1.2, were produced. For the flat substrate S_0, measurements for $a_{p,0} = 1.0 \text{ mm}$ were not carried out.

Figures 4.8 and 4.9 show the wave evolution for all four substrates, the seven frequencies and the paddle amplitude $a_{p,0} = 4.0 \text{ mm}$. The waves are much larger than in the linear regime and do not show a sinusoidal profile. The waves

over the flat substrate all decay on their way down the channel. Together with figure 4.2, this shows that the waves' growth or decay does also depend on their amplitude. In the linear theory, the amplitude was always set to zero and so the growth did only depend on the Reynolds, Kapitza and wave number (see sections 3.2 and 4.1.2).

Also the shape of the wave was restricted to sinusoidal in the linear regime.
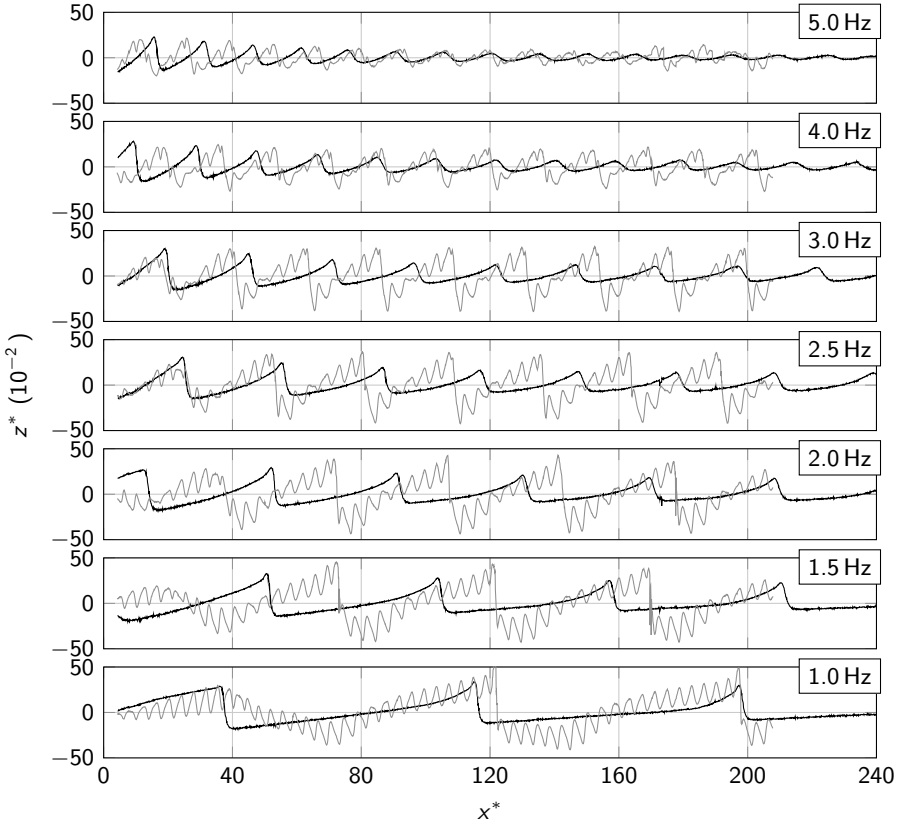

Figure 4.8: The wave's shape $h_c^*(x^*, t^*)$ at a random time for S_0 (black) and S_1 (gray), $Ka = 2.01$, $Re = 11.9$, $a_{p,0} = 4.0$ mm and all seven paddle frequencies.

Nonlinear waves change their shape on the way down the channel by transferring energy to higher harmonics of the paddle frequency. The shapes of the waves over the different substrates show qualitative similarities, if the dents caused by the substrate's undulations are ignored: All waves have a steep front and a gently falling tail. The lower the paddle frequency, the steeper the front is. Taking a closer look at the tails, they exhibit a concave shape for the waves over
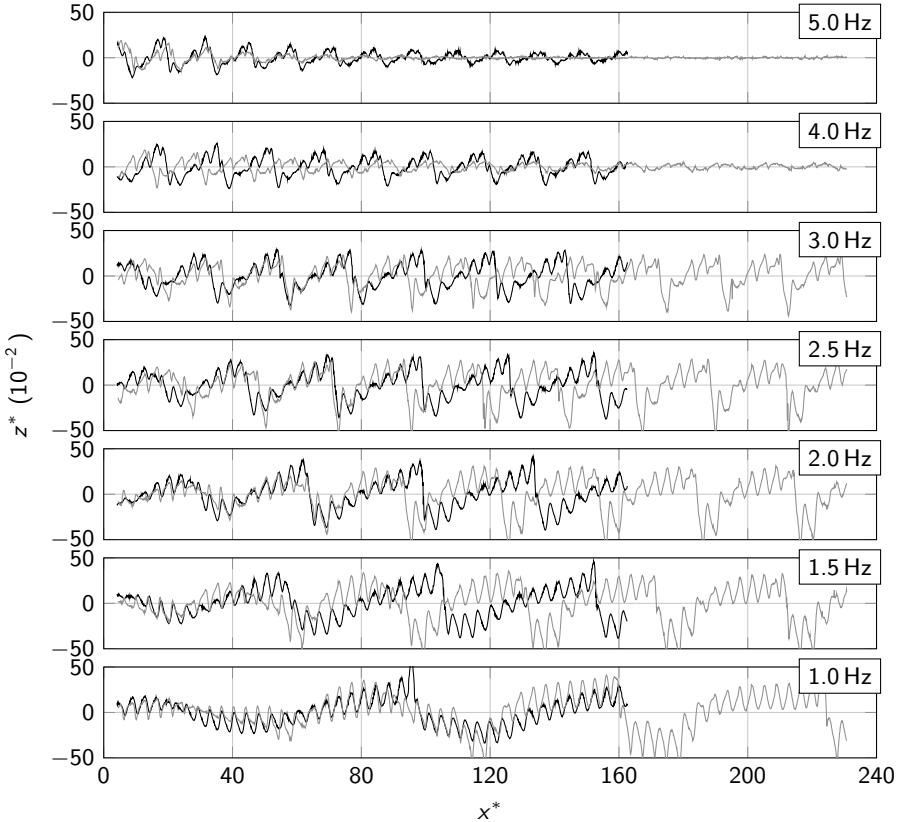

Figure 4.9: The wave's shape $h_c^*(x^*, t^*)$ at a random time for S_2 (black) and S_3 (gray), $Ka = 2.01$, $Re = 11.9$, $a_{p,0} = 4.0\,\text{mm}$ and all seven paddle frequencies.

the flat substrate, while the ones over all undulated substrates exhibit a convex shape. It also looks like most waves over the undulated substrates reached a saturation state, where they do neither change their amplitude, nor their shape beyond a certain traveling distance. On the other hand, the waves over the flat substrate are still decaying at the most downstream position ($x^* = 240$).

These qualitative observations were quantified by going to the frequency space via a Fast Fourier Transformation (*MATLAB* function `fft()`) of the amplitude-time signal at every position in x^*-direction. An example for S_0, $a_{p,0} = 4.0\,\text{mm}$ and $f_p = 3.0\,\text{Hz}$ at $x^* = \{4, 240\}$ is plotted in figure 4.10. It shows the decay of the amplitude of the first and higher harmonic frequencies. This is also displayed in figure 4.11, where the amplitude of the first three harmonics is drawn against the x^*-coordinate exemplarily for S_0 and S_1, $a_{p,0} = \{0.25, 1.0, 4.0\}\,\text{mm}$ and $f_p = \{1.0, 3.0, 5.0\}\,\text{Hz}$. It is important to note here that the amplitude evolution over S_1 was averaged over a substrate's wavelength, because the amplitude of a wave depends on the position inside a substrate's wavelength (dents in figures 4.8 and 4.9). As in the linear regime, the development of the waves over the undulated substrate happens much faster than for the flat one (compare to [108]). The amplitudes of the first three harmonics over S_1 do not change significantly over the last $200\,\text{mm} = 37.7 \times d_n$ of the channel and hence reached saturation. It can also be stated that the saturation amplitude a^*_{sat} does not depend on the initial amplitude of the wave, but only on its frequency.

For the flat substrate, saturation is mostly not yet reached at the end of the channel. According to Liu et al. [79] and Alekseenko et al. [81], the waves that flow over the flat substrate will eventually reach a steady state somewhere downstream. Since that state is neither reached by the waves generated with $a_{p,0} = 0.25\,\text{mm}$ nor the ones generated with $a_{p,0} = 4.0\,\text{mm}$, it was only possible to give upper and lower boundaries for their saturation amplitude a^*_{sat}. These were calculated by fitting a linear function to the wave's amplitude for the last $200\,\text{mm} = 37.7 \times d_n$ of the measurement area. If the slope of this function was positive, the amplitude at the most downstream position gave a lower boundary for a^*_{sat}, if the slope was negative, an upper boundary was at hand.

Aside from the waves over the flat substrate, the amplitudes of the first three harmonics of all other waves generated with $a_{p,0} = 1.0\,\text{mm}$ or $a_{p,0} = 4.0\,\text{mm}$ reached saturation. The wave number k^*_c in the state of saturation was deter-
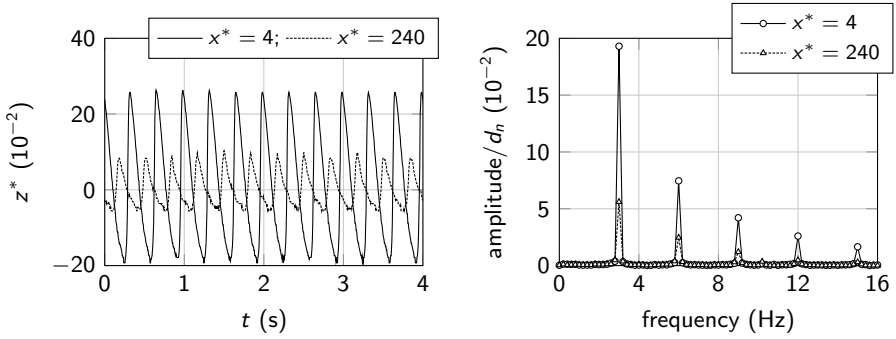
Figure 4.10: Left: The wave's amplitude-time signal exemplarily for S_0, $a_{p,0} = 4.0$ mm and $f_p = 3.0$ Hz at the most upstream $(x^* = 4)$ and most downstream $(x^* = 240)$ position. Right: The amplitude spectra of the signals, computed by a Fast Fourier Transformation.
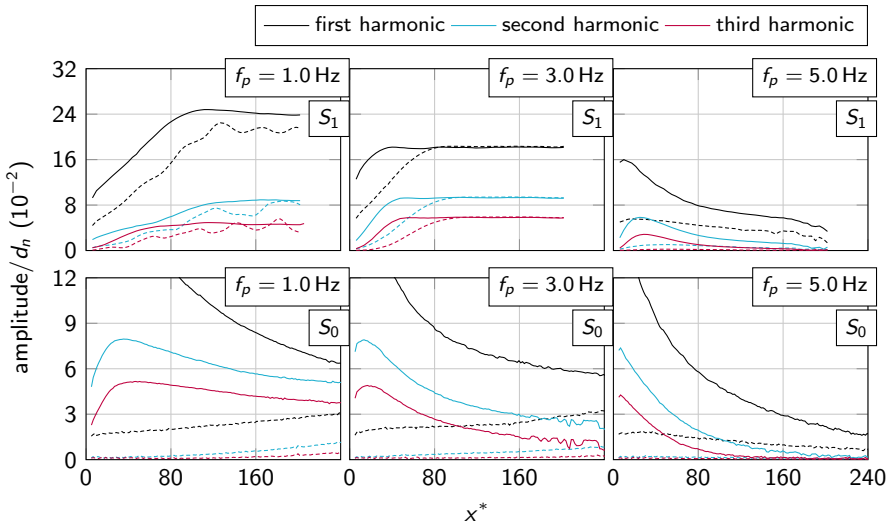

Figure 4.11: The evolution of the amplitudes of the first, second and third harmonic exemplarily for S_0 and S_1 and for three frequencies. Solid lines indicate that the paddle's amplitude is $a_{p,0} = 4.0$ mm, dashed lines $a_{p,0} = 0.25$ mm for S_0 and $a_{p,0} = 1.0$ mm for S_1. The small wiggles in the plots are due to noise effects in the experiments.

mined by the phase difference in radian measure between two points in stream
wise direction which were 40 mm (or two substrate wavelengths) apart:

$$k_c^* = \frac{\text{phase difference} \cdot d_n}{40\,\text{mm}}. \tag{4.11}$$

This was also carried out for the waves over the flat substrate, although sat-
uration was not yet reached. Yet, the wave numbers of the upper and lower
boundary saturation amplitudes differed less than the estimated error for k_c^*.

Figure 4.12 reveals the dependence of the saturation amplitude a_{sat}^* on the wave
number k_c^*. Concerning the flat substrate S_0, the first harmonic reached the
highest saturation amplitude for the wave number that also had the highest
growth rate (figures 4.3 and 4.7). For the wave number close to the critical
one (growth rate = zero, from the Orr-Sommerfeld equation), the saturation
amplitude of the first harmonic tends to zero. Thus, if the wave number lies
beyond the critical one, all waves of the same wave number, arbitrary shape
and amplitude will eventually vanish on their way down the channel. This also
shows that for measurements of the linear stability of film flows, it might be
more accurate to determine the critical wave number as the one, where the
saturation amplitude a_{sat}^* of the first harmonic tends to zero, instead of where
the growth rate b^* is zero (compare figures 4.3 and 4.12). As already discussed
in section 4.1.2, using $b^* = 0$ as the condition for the critical wave number
would only be accurate, if the amplitude of the wave was zero. But this is
experimentally not doable. The amplitudes of the second and third harmonics
do not necessarily tend to zero beyond the critical wave number. Energy is
transferred from the first harmonic to the higher ones and so the amplitudes
of the higher harmonics do not vanish. That leads to an equilibrium between
the amplification of the first harmonic and the energy transfer to the higher
harmonics which are damped if they lie beyond the critical wave number.

The data for the saturation amplitudes of waves over the undulated substrates
show that, apart from a much higher growth rate, the waves also exhibit a
much higher saturation amplitude than the waves over the flat substrate. Also
the amplitude of waves that show a negative growth rate in figure 4.7, do not
necessarily go to zero. This again is a proof for the error made, if the critical
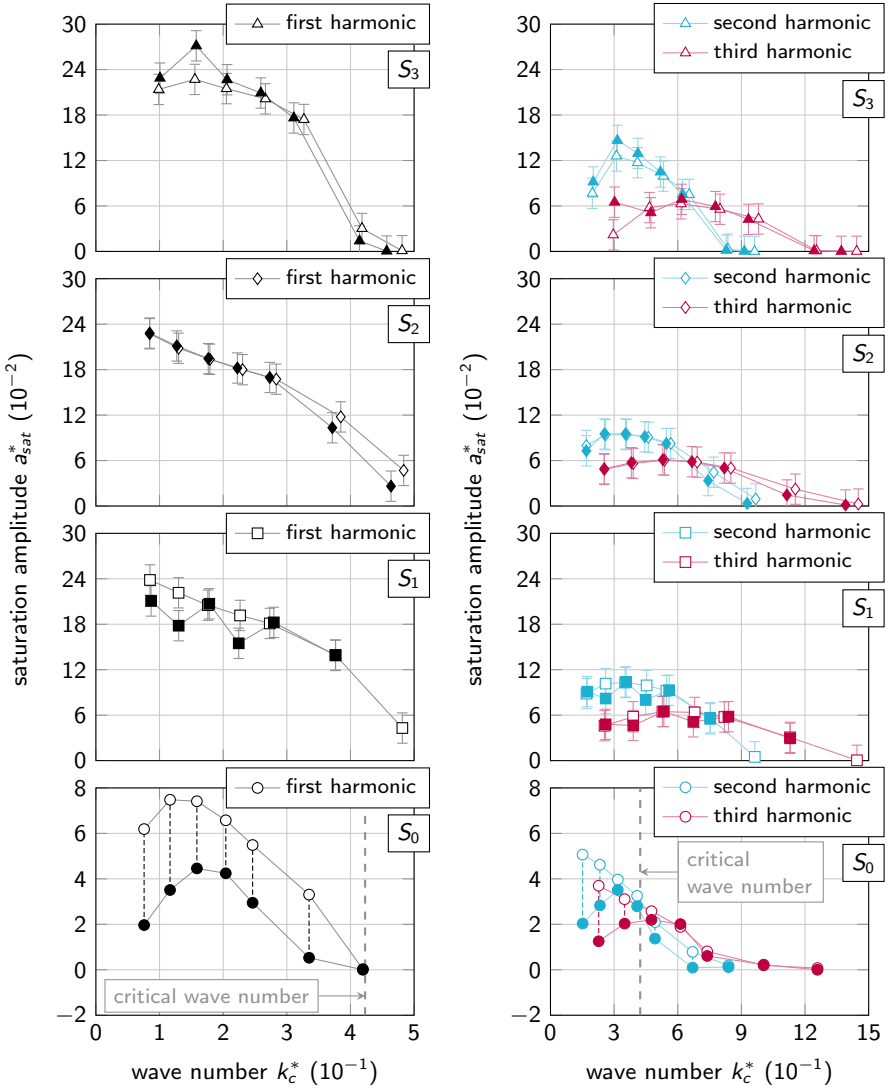wave number is determined by the experimental measurement of the growth

Figure 4.12: The saturation amplitudes a_{sat}^* for all substrates and frequencies. For S_0, only upper (open symbols) and lower (solid symbols) boundaries for a_{sat}^* are given. For $S_1 - S_3$, the open symbols indicate $a_{p,0} = 4.0\,\text{mm}$, the solid symbols $a_{p,0} = 1.0\,\text{mm}$.

rate. Aside from that, the saturation amplitude does for all wave numbers not depend on the paddle amplitude. The saturation amplitudes of the waves over S_1 and S_2 are almost equal and it stands out that the highest saturation amplitude is not at the same wave number as the highest growth rate (figure 4.7). For the rectangular substrate S_3, the highest saturation amplitude is also slightly shifted compared to the highest growth rate, but not as much.

There is a very distinct difference between the saturation states of the waves over a flat and an undulated substrate. While waves over a flat substrate will eventually reach a steady state, if observed in a coordinate system that moves with the waves' speed, the undulations make this impossible. If the same moving coordinate system is used, the lower boundary of the observed domain changes periodically. Hence no steady state can be reached for waves over undulated substrates. Only if the amplitude is averaged over a substrate's wavelength, one can determine a saturation state, but not a real steady state.

4.2 Solitary wave dynamics

The dynamics of solitary waves has been studied by several authors, e.g. [48, 76, 77, 79, 82–87]. These authors define solitary waves as a limit case of continuous waves. For example, Liu et al. [48] defined the transition between "saturated finite amplitude waves (at high f[requencies])" and "multipeaked solitary waves (at low f[requencies])". They defined the waves as solitary waves, if there is a small loop in the phase orbit (the $\partial h/\partial x$ - $\partial^2 h/\partial x^2$-plane). Argyriadi et al. [77] defined solitary waves as "localized structures separated by relatively long stretches of substrate". But they still use "constant-frequency disturbances at the channel inlet, with the aim of producing a regular wave train." Similar to Alekseenko et al. [81], the measurements in this work were done by generating exactly one initial solitary wave with a certain length and amplitude and not a wave train.

4.2.1 The evolution of solitary waves

For the measurements of the evolution of solitary waves, the oil *Elbesil 65* (parameters in table 2.1) was filled into the flow circuit (figure 2.1). The solitary

wave dynamics were only measured over the flat substrate S_0. The temperature was set to

$$\theta = (23.0 \pm 0.2)\,^{\circ}\mathrm{C} \tag{4.12}$$

and the inclination angle to

$$\alpha = (10.0 \pm 0.1)\,^{\circ}. \tag{4.13}$$

The volume flux was tuned to a constant value of

$$\dot{V} = (115 \pm 3)\,\frac{\mathrm{cm}^3}{\mathrm{s}}. \tag{4.14}$$

Then the corresponding Nusselt film thickness, free surface velocity and Reynolds number were calculated by using equations 2.2, 2.3 and 2.5:

$$d_n = (4.3 \pm 0.1)\,\mathrm{mm} \tag{4.15}$$

$$u_s = (227 \pm 6)\,\frac{\mathrm{mm}}{\mathrm{s}} \tag{4.16}$$

$$Re = 15.0 \pm 0.5. \tag{4.17}$$

Contrary to the experiments in section 4.1, the paddle at the inlet of the channel produced exactly one solitary wave, by running the function in equation 2.7 only once and not continuously. Hence it does not make sense to define a paddle frequency but rather the period T_p of the paddle movement. Also, the paddle started at its lowermost position. Then equation 2.7 changes to

$$a_p(t) = a_{p,0}\left(1 - \cos\left(\frac{2\pi}{T_p}t\right)\right). \tag{4.18}$$

The experiments were carried out at four different paddle amplitudes

$$a_{p,0} = \{0.05, 0.25, 1.0, 4.0\}\,\mathrm{mm} \tag{4.19}$$

and eight different periods

$$T_p = \{1000, 500, 333, 250, 200, 167, 143, 125\}\,\mathrm{ms}. \tag{4.20}$$

Before the movement of the paddle started, it was dipped into the oil and so some of the liquid was impounded behind the paddle (figure 4.13). Once the paddle movement started, the impounded liquid was released and formed a solitary wave, whose development down the channel was then recorded by the setup described in section 2.2.2.
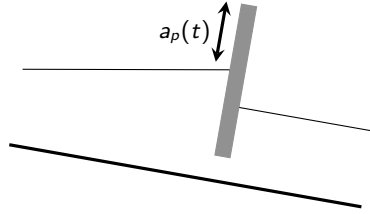

Figure 4.13: Paddle with the impounded liquid, $a_p(t) = a_{p,0}\left(1 - \cos\left(2\pi t/T_p\right)\right)$. Reproduced with permission from [98]. ©2015, AIP Publishing LLC.

Figure 4.14 shows the evolution of a solitary wave, created with the paddle amplitude $a_{p,0} = 0.05\,\mathrm{mm} = 0.012 \times d_n$. Since the solitary wave is only located at a certain area of the channel, only this area is plotted. Each graph shows the solitary wave at three different times and since the wave travels downstream also at three different locations. The waves with shorter periods ($T_p = \{143, 250\}\,\mathrm{ms}$) exhibit the same qualitative behavior: Shortly behind the inlet at time t_0, they have a sinusoidal shape and directly in front of and behind the waves, the film returns to the flat Nusselt solution. Further downstream, at time $t_0 + 2.16\,\mathrm{s}$, the waves are slightly distorted and behind the main waves, secondary ones appear. This phenomenon was described as "parasitic waves" by Argyriadi et al [77]. At the last time step, the solitary waves changed their shape from sinusoidal to saw-tooth-like with a steep front and a gently falling tail which was also observed for nonlinear continuous waves of low frequencies in section 4.1. When the solitary wave was produced with the period $T_p = 500\,\mathrm{ms}$, a slightly different shape is formed: The wave does not show a sinusoidal profile, but has a flat top. At the second time step, the wave has already developed a saw-tooth-like shape and also the parasitic wave behind the first one. These features solidify themselves at the third position. A completely different wave profile is developed, when the paddle period is increased to $T_p = 1000\,\mathrm{ms}$. At

t_0, a wave profile with a flat top which has the length of about $50 \times d_n$ is visible. This area can be approximated as a Nusselt film with a film thickness of $d_n + h_s(x^* \approx 50)$ which is very unstable, since the basic flow is already unstable. This instability leads to a separation of the solitary wave into two waves at $t_0 + 2.16\,\mathrm{s}$ (compare to Alekseenko et al. [81]). This trend continues to the third position, where also the parasitic wave is visible behind the divided solitary wave. For $T_p = 500\,\mathrm{ms}$ the flat top of the solitary wave at the first position was not long enough (about $25 \times d_n$) to be considered as a Nusselt flow with a higher film thickness and thus did not command a separation of the solitary wave into two waves.
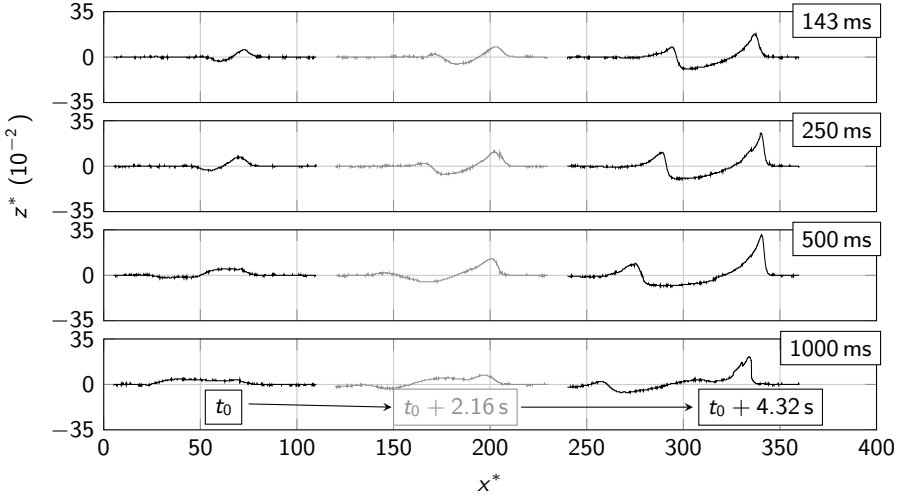

Figure 4.14: The wave's shape $h_s^*(x^*, t^*)$ at three time steps t_0, $t_0 + 2.16\,\mathrm{s}$ and $t_0 + 4.32\,\mathrm{s}$ and hence three different x^*-locations. $Ka = 3.54$, $Re = 15$, $a_{p,0} = 0.05\,\mathrm{mm}$ and four paddle periods.

The solitary waves that were created with the paddle amplitudes $a_{p,0} = 1.0\,\mathrm{mm} = 0.23 \times d_n$ and $a_{p,0} = 4.0\,\mathrm{mm} = 0.93 \times d_n$ are shown in figures 4.15 and 4.16, respectively. Similar to figure 4.14, a saw-tooth-like shape is visible, with a steepening front until it is almost perpendicular to the basic flow's free surface. Also, the parasitic waves behind the solitary waves are present for all paddle

periods. On their way down the channel, the parasitic waves grow in amplitude, and the distance to the solitary waves becomes noticeably larger at the same time. Since the liquid film in front of the parasitic waves has a lower free surface height than the film in front of the solitary waves, their velocities and saturation amplitudes have to differ significantly. This leads to wave packages that consist of: the solitary wave → a depression area → the parasitic wave → possibly another depression area, depending on the amplitude of the parasitic wave. The system of the solitary and the parasitic wave can never reach a steady state, because the depression area between the two will always grow.

Likewise, the distance between the separated waves (e.g. figure 4.15, $T_p = 1000\,\text{ms}$) increases due to the different amplitudes the separated waves have. This is accompanied by a deepening of the dent between these two waves. The wave package in this case consists of: the first part of the separated wave (from here on referred to as the solitary wave) → a small depression area which grows in width and depth on its way downstream → the second part of the separated wave (from here on referred to as the secondary wave) → a depression area → the parasitic wave → possibly another depression area, depending on the amplitude of the parasitic wave.

So, depending on the initial conditions of the solitary waves, two qualitatively different developments of the waves are possible. It seems like the important condition is not the amplitude of the initial wave, but its length. All waves created with a paddle period of 1000 ms feature a separation into two waves, but none with a lower T_p (figures 4.14 - 4.16). Since the difference between the highest two paddle periods (1000 ms to 500 ms) is very large, no definite statement is possible. Overall, the combined contribution of the solitary wave and successive waves and depressions to the flow rate has to be zero, because after the paddle finished its movement, the basic flow has to be reestablished.

It is important to note that there are no waves preceding the solitary wave. They were numerically and experimentally observed by several authors, e.g. [76, 77, 79, 81, 82, 109] and were called "capillary ripples" which require high Kapitza numbers. Here, the Kapitza number is about three magnitudes lower than in the aforementioned publications, where aqueous solutions were used.
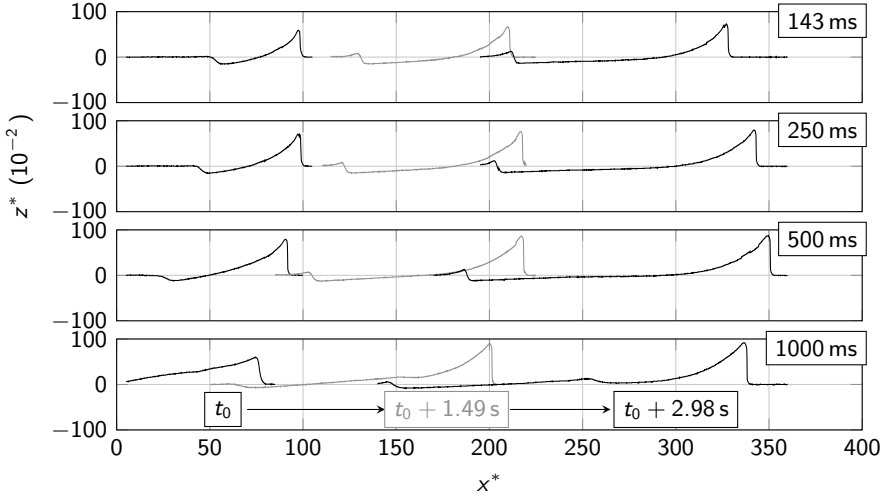
Figure 4.15: The wave's shape $h_s^*(x^*, t^*)$ at three time steps and hence three different x^*-locations. $Ka = 3.54$, $Re = 15$, $a_{p,0} = 1.0\,\text{mm}$ and four paddle periods.
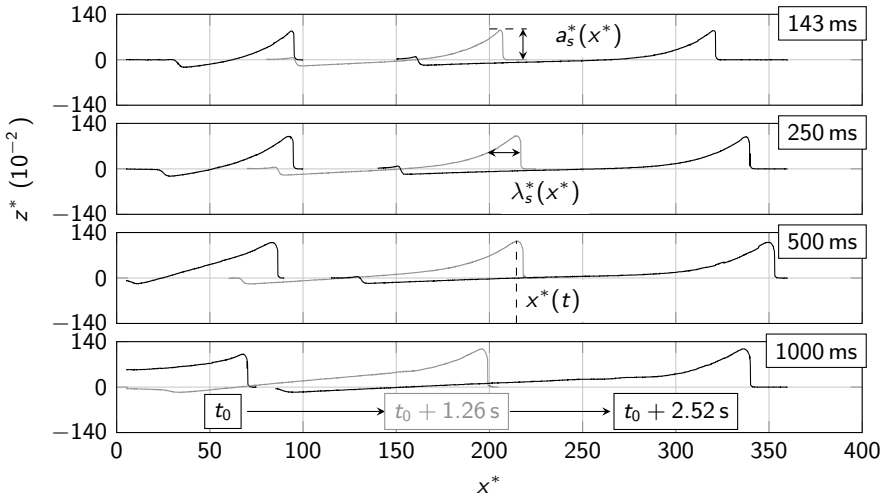

Figure 4.16: The wave's shape $h_s^*(x^*, t^*)$ at three time steps and hence three different x^*-locations. $Ka = 3.54$, $Re = 15$, $a_{p,0} = 4.0\,\text{mm}$ and four paddle periods.

The development of the solitary wave is further examined in the following. For that, in figure 4.16, three key parameters are defined: The wave's amplitude $a_s^*(x^*)$, its length $\lambda_s^*(x^*)$ at $a_s^*/2$ (full length at half maximum) and its position $x^*(t^*)$. The first derivative of $x^*(t^*)$ gives the phase velocity $v_s^*(x^*)$.

The evolution curve of the solitary wave's amplitude $a_s^*(x^*)$ is shown in the uppermost row of figure 4.17. For the smallest paddle amplitude ($a_{p,0} = 0.05\,\text{mm}$), all waves grow monotonously and qualitatively equally. For the paddle amplitudes $a_{p,0} = 1.0\,\text{mm}$, the amplitude first grows rapidly until a buckle is reached. Then the growth is slowed down and even becomes negative in some cases. Then the amplitude starts growing again, until a threshold of $a_s^* \approx 0.9$ is reached. When setting the paddle amplitude to $a_{p,0} = 4.0\,\text{mm}$, the first rapid growth does not take place, since the initial amplitude of the wave is already very high. Depending on the paddle period, the wave first either grows or shrinks and then approximates the aforementioned threshold.

During the rapid growth of the amplitude, the length λ_s^* of the solitary wave decreases just as quickly (figure 4.17, center row, $a_{p,0} = 1.0\,\text{mm}$). Once the shortening becomes less pronounced, the growth of the amplitude slows down. It even becomes negative, if the wave's length increases again ($a_{p,0} = 1.0\,\text{mm}$ and $a_{p,0} = 4.0\,\text{mm}$). As soon as the wave's length does not change as much, the amplitude of the wave moves towards the aforementioned threshold of $a_s^* \approx 0.9$.

The wave's velocity v_s^* (figure 4.17, lowermost row) depends heavily on the paddle amplitude: the higher the amplitude, the higher the velocity. The dependency of the wave's velocity on its amplitude is well documented in the literature, e.g. [79, 81, 89] and visible, if one compares the uppermost and lowermost rows in figure 4.17. In order to do this, the mean velocity and mean amplitude for each of the measured solitary waves beyond $x^* = 300$, where most parameters became constant, were calculated and plotted in figure 4.18. The graph shows a monotonous increase of the wave's velocity with its amplitude. But, other than reported by some of the aforementioned papers, the dependency is not linear. This can have the following reasons: Firstly, the waves measured in this work did not always reach a steady state, and are still developing beyond $x^* = 300$, as can be seen in figure 4.17. This effect is rather small, though: On the right hand side of figure 4.18, the errors Δv_s^* and Δa_s^* were estimated by computing the standard deviations over the averaged
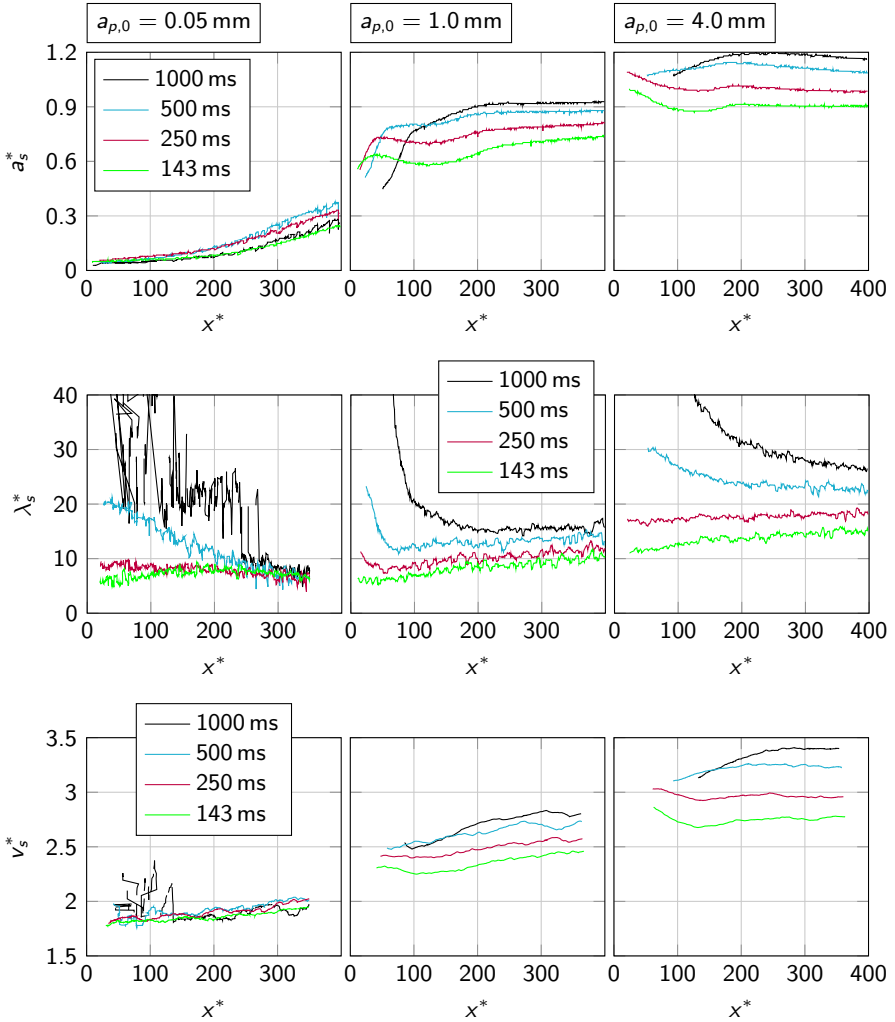
Figure 4.17: The evolution of a solitary wave's amplitude a_s^* (top row), length λ_s^* (middle row) and velocity v_s^* (bottom row) for three different paddle amplitudes $a_{p,0} = \{0.05, 1.0, 4.0\}$ mm (from left to right) and four paddle periods. The first part of the black curve on the left hand side of the λ_s^* evolution is overlain by heavy noise, because of the break-up mechanism of the solitary wave (see figure 4.14).

values. The error is always smaller than five percent of the respective mean value. Secondly, the results obtained in [79, 89] are exclusively for wave trains and not for single solitary waves that were scrutinized for this dissertation. These "truly solitary waves" are not confined by preceding and succeeding waves and can so develop freely not only in the z^*- but also in the x^*-direction (figures 4.14 through 4.17). This seems to have a decisive impact on the wave's velocity. Alekseenko et al. [81] suggested to use a quadratic function instead of a linear one. This was derived from the assumption that the velocity profile inside a solitary wave is also quadratic. Regarding the extremely steep front of the solitary waves (figures 4.15 and 4.16), it seems very unlikely that this is the case for the present waves. Though it is possible to fit a quadratic function $v_s^*(a_s^*) = 1.07a_s^{*2} + 1.91$ to the data in figure 4.18, this function is not in agreement with the derived one in [81]: $v_s^*(a_s^*) = a_s^{*2} + 2a_s^* + 2$.
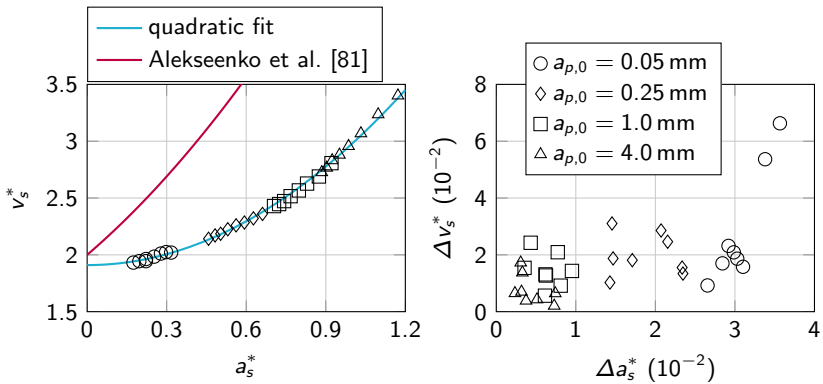

Figure 4.18: Left: The velocity v_s^* vs a_s^*. Both are mean values computed from the waves which nearly reached saturation ($x^* \geq 300$). All paddle amplitudes (equation 4.19) and paddle periods (equation 4.20) are considered. **Right:** The standard deviations of a_s^* and v_s^*.

4.2.2 Streamlines underneath solitary waves

When the waves grow in amplitude, the velocity of the fluid directly at the free surface should also become higher, since it is farther away from the substrate (see e.g. [81]). Simultaneously, also the velocity of the solitary waves grows with its amplitude (figure 4.18). If there were a point where the highest velocity in the fluid becomes larger than the wave's velocity, the question arises, why the waves do not break at that point.
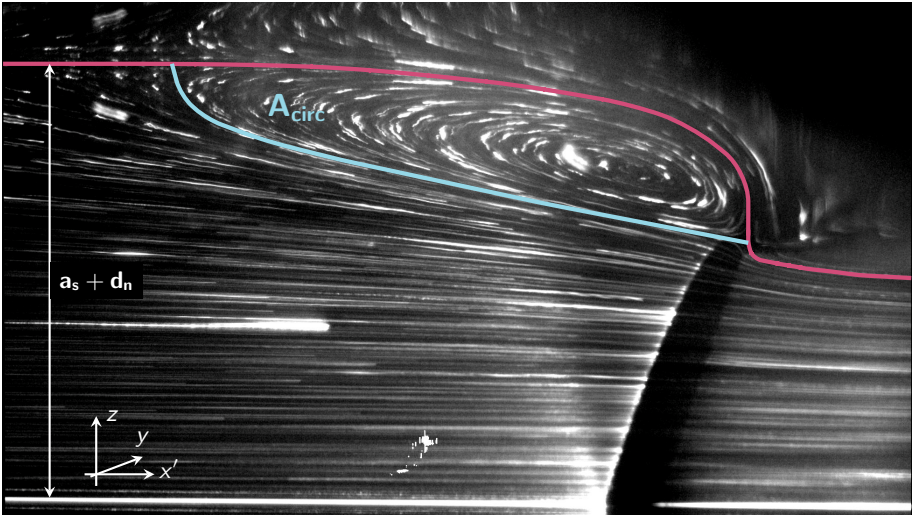

Figure 4.19: Example for streamlines in a reference frame $(x' = x - v_s t, y, z)$ that moves with the speed v_s of the solitary wave. The free surface of the liquid reflected the streamlines, thus there are streamlines visible above the free surface. This made it possible to localize the free surface and mark it with a purple line. The cyan line shows the separation between the recirculation area which lies directly at the free surface of the wave, and the flowing film. The recirculation runs clockwise and the flowing film below goes from right to left, due to the moving coordinate system. The wave's amplitude a_s and the size of the recirculation area A_{circ} were measured. The black area below the wave front is a shadow from the laser light casted by the wave front. Reproduced with permission from [98]. ©2015, AIP Publishing LLC.

These open questions were tackled by visualizing the streamlines underneath the free surface of the solitary waves. The idea behind this came from several numerical predictions of recirculation areas that appear underneath a solitary wave, when it is regarded in a reference frame that moves with the wave's speed [71, 84, 86, 110–113]. This explains, how the velocity of a fluid particle can become higher than the wave's velocity without a wave breaking.

Since there was no experimental prove that these recirculation areas indeed exist, Reck and Aksel [98] used the setup described in section 2.2.2 to record the streamlines underneath a solitary wave in a reference frame that moved with the wave's speed v_s. The experimental confirmation for the existence of recirculation areas underneath large solitary waves is shown in figure 4.19. The recirculation area lies directly underneath the free surface and its center is located in the front part of the wave. In figure 4.20, the streamlines of three solitary waves with different amplitudes a_s^* are shown. Because the same paddle amplitude of $a_{p,0}/d_n = 1.16$ was used for all three pictures, the different amplitudes are the consequence of different paddle periods $T_p u_s/d_n = \{10.9, 16.3, 27.2\}$. The recirculation areas do not appear, if the wave's amplitude a_s^* ist too small, as is the case in the uppermost picture. If the amplitude is sufficiently large, a recirculation area is visible (middle and lowermost picture of figure 4.20). Furthermore, the size of the recirculation area is bigger for a larger amplitude. The numerical computations published in [71, 84, 86, 110, 111] predict that the recirculation area appears underneath the wave peak and not directly behind the front of the wave as in the recordings in figure 4.20. The main difference to the experiments in this dissertation is the Kapitza number. The experiments here were carried out with silicon oil with $Ka = 3.54$, whereas the numerical calculations in the forecited papers dealt with aqueous solutions and $Ka = O(10^3)$.

Rohlfs and Scheid [112] predicted via a weighted integral boundary layer model that the onset of recirculation areas underneath free surface waves depends only on the wave amplitude to film thickness ratio. In order to test this, the wave's amplitude a_s and the size of the recirculation area A_{circ} were extracted from the streamline pictures by visual judgment (figure 4.19). Since the speed of the moving reference frame (consisting of a camera and a laser mounted on a movable platform, see section 2.2.2) was set equal to the wave's speed, v_s was
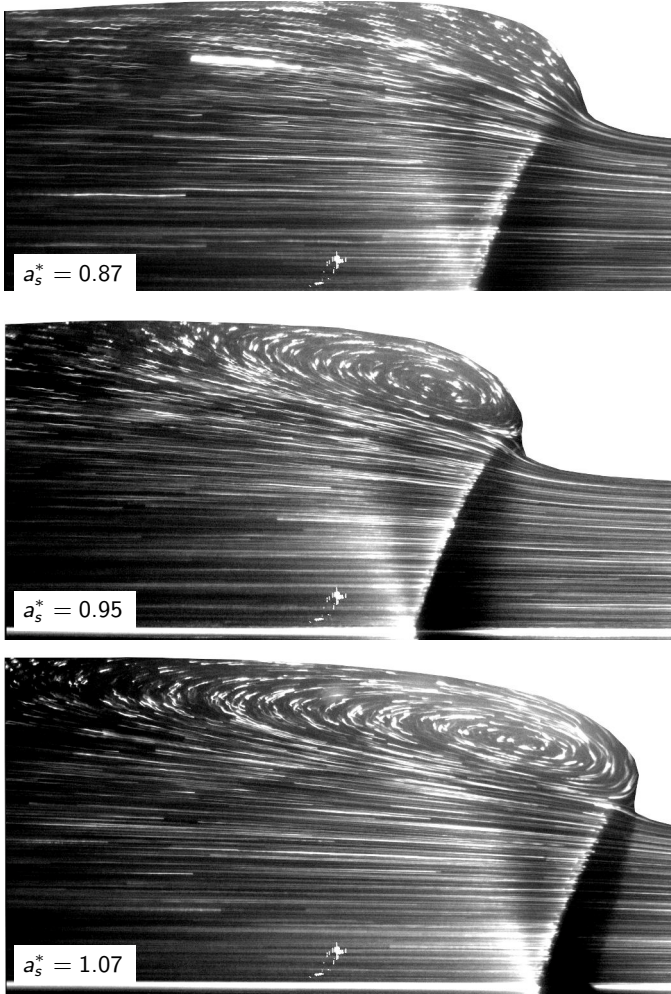
Figure 4.20: Exemplary streamlines of waves over a film flow of $Re = 15$, $\alpha = 10\,^{\circ}$ at $x^* = 350$. The parts of the images above the free surfaces were removed (compare to figure 4.19). Paddle amplitude $a_{p,0}/d_n = 1.16$. Top, $T_p u_s/d_n = 10.9$: no recirculation area appears because the wave's amplitude is too small. Middle, $T_p u_s/d_n = 16.3$ and bottom, $T_p u_s/d_n = 27.2$: recirculation area appears and its size depends on the wave's amplitude. Reproduced with permission from [98]. ©2015, AIP Publishing LLC.

also noted. The measurements of the wave's amplitude a_s and phase velocity v_s in section 4.2.1 could only be used as a qualitative guideline, because a different paddle was used for the generation of the solitary waves, as described in section 2.2.2. A variety of initial solitary waves were produced by setting seven different dimensionless paddle periods $T_p u_s / d_n$ between 11 and 71, and five different dimensionless paddle amplitudes $a_{p,0}/d_n$ between 0.21 and 1.5. The results were improved by recording six images per setting and calculating the mean values to receive A_{circ} and a_s. The uncertainties in the measurements of the size of the recirculation area ΔA_{circ} and the wave's amplitude Δa_s were determined by the standard deviation. The non-dimensional values were:

$$A_{circ}^* = \frac{A_{circ}}{d_n{}^2}, \tag{4.21}$$

$$a_s^* = \frac{a_s}{d_n}, \tag{4.22}$$

and the respective errors:

$$\Delta A_{circ}^* = \frac{\Delta A_{circ}}{d_n{}^2}, \tag{4.23}$$

$$\Delta a_s^* = \frac{\Delta a_s}{d_n}. \tag{4.24}$$

These errors were obtained by using the largest respective standard deviation, since the measurements were done by visual judgment. Additionally, the amplitude of the solitary wave changed slightly during the recording time of $1/21\,\mathrm{s}$. The wave traveled less than $50\,\mathrm{mm} \approx 12 \times d_n$ during that timespan. The positions in which the streamlines were recorded were at $x \approx 900\,\mathrm{mm}$ and $x \approx 1500\,\mathrm{mm}$ (in dimensionless values: $x^* = 210$ and $x^* = 350$ for $Re = 15$, $\alpha = 10\,°$). The top row of figure 4.17 shows a maximal change in amplitude of 0.015 over these parts of the channel. Together with the standard deviations from the six measurements, the errors are:

$$\Delta A_{circ}^* = 0.2 \tag{4.25}$$

$$\Delta a_s^* = 0.02. \tag{4.26}$$

First, the influence of the initial conditions of the solitary wave, i.e. the paddle period and amplitude, on the size of the recirculation area was scrutinized.

The same basic flow was set up as in section 4.2.1 by keeping the Reynolds number at $Re = 15$ and the inclination angle at $\alpha = 10\,^\circ$. It was revealed in section 4.2.1 that the initial conditions influence the wave's amplitude at the measurement positions. Aside from that, do they influence the size of the recirculation areas in another way?
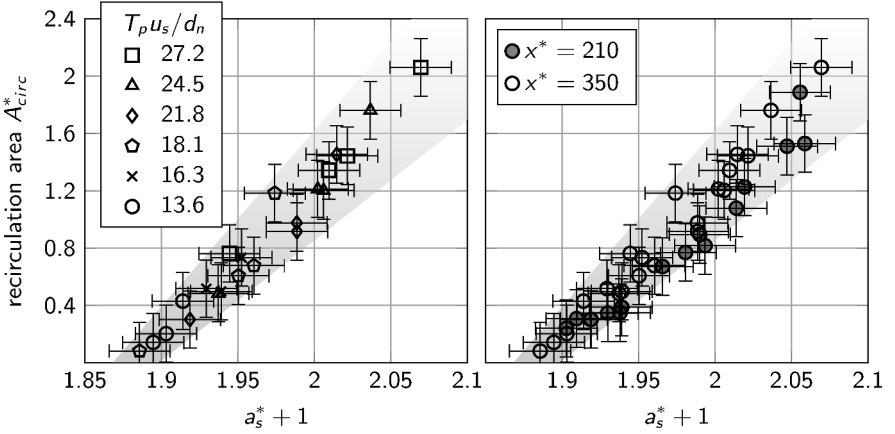

Figure 4.21: The relative size A_{circ}^* vs $a_s^* + 1$ for $\alpha = 10\,^\circ$, $Re = 15$. **Left:** Different dimensionless paddle periods $T_p u_s / d_n$ at $x^* = 350$. The different wave amplitudes a_s^* are the result of different paddle amplitudes $a_{p,0}/d_n = \{0.46\,,0.71\,,0.93\,,1.16\,\}$.
Right: Different locations in stream wise direction. The two graphs indicate that A_{circ}^* depends neither on the initial conditions at the inlet, nor on the location in stream wise direction, but only on a_s^*. Reproduced with permission from [98]. ©2015, AIP Publishing LLC.

The left graph of figure 4.21 shows the size of the recirculation areas plotted against the wave's amplitude for $x^* = 350$ and all paddle periods and amplitudes. Different symbols represent different paddle periods. The paddle amplitudes are not distinguished in this plot. Generally, a higher paddle amplitude led to a higher amplitude at the measurement position. The graph indicates that the initial conditions of a wave do not influence the size of the recirculation area aside from their influence on the wave's amplitude. On the right hand side of figure 4.21, the dependency of A_{circ}^* on a_s^* is displayed for the same parameters and for both measurement positions $x^* = \{210, 350\}$. From

this plot can be concluded that the size of the recirculation area also does not depend on the measurement position.

Next, the influence of changes to the basic flow on the recirculation area was investigated. In a first step the Nusselt film thickness and free surface velocity were modified by changing the inclination angle to $\alpha = 15°$. Equations 2.2 and 2.3 then led to

$$d_n = (3.8 \pm 0.1)\,\text{mm} \tag{4.27}$$

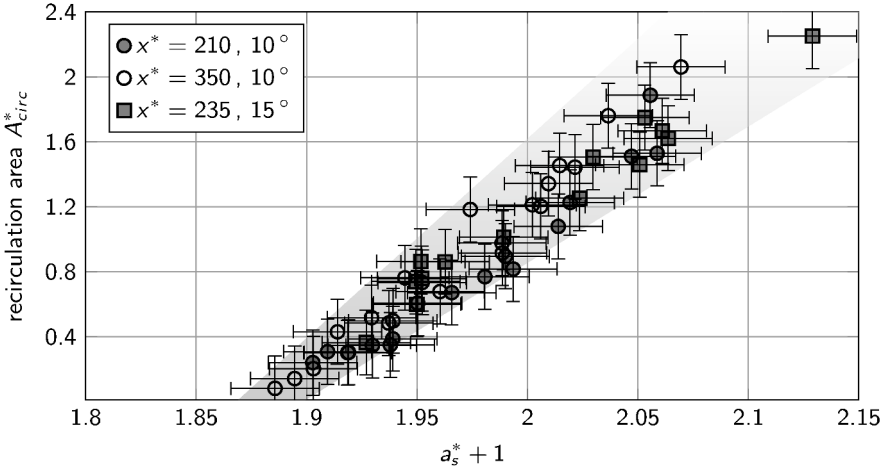$$u_s = (268 \pm 6)\,\frac{\text{mm}}{\text{s}}. \tag{4.28}$$

Figure 4.22: The relative size A_{circ}^* vs $a_s^* + 1$ for $Re = 15$: Though the basic flow is different for $\alpha = 15°$ compared to $\alpha = 10°$, the dependency of A_{circ}^* on a_s^* is the same. Reproduced with permission from [98]. ©2015, AIP Publishing LLC.

In this case, the measurements took place at $x \approx 900\,\text{mm}$, or in dimensionless representation, at $x^* \approx 235$. The evolution of the solitary wave was not measured, but it is a sensible assumption that the wave's amplitude did not change significantly during a streamline measurement similar to the case for $\alpha = 10°$. The results are plotted in figure 4.22 and show that the size of the recirculation

area still shows the same dependency on the wave's amplitude as for $\alpha = 10°$, though the basic flow was changed.

In a second step, the basic flow was adjusted by changing the Reynolds number to 10 and 20 for both inclination angles $\alpha = \{10, 15\}°$ and both measurement positions $x = \{900, 1500\}$ mm. Since the Nusselt film thickness differed for the altered Reynolds numbers and inclination angles, the measurement positions in dimensionless representation also varied. Figure 4.23 shows the size of the recirculation area plotted against the wave's amplitude for all measured parameters. It is shown that the correlation between A^*_{circ} and a^*_s is neither influenced by the inclination angle nor by the measurement position in stream
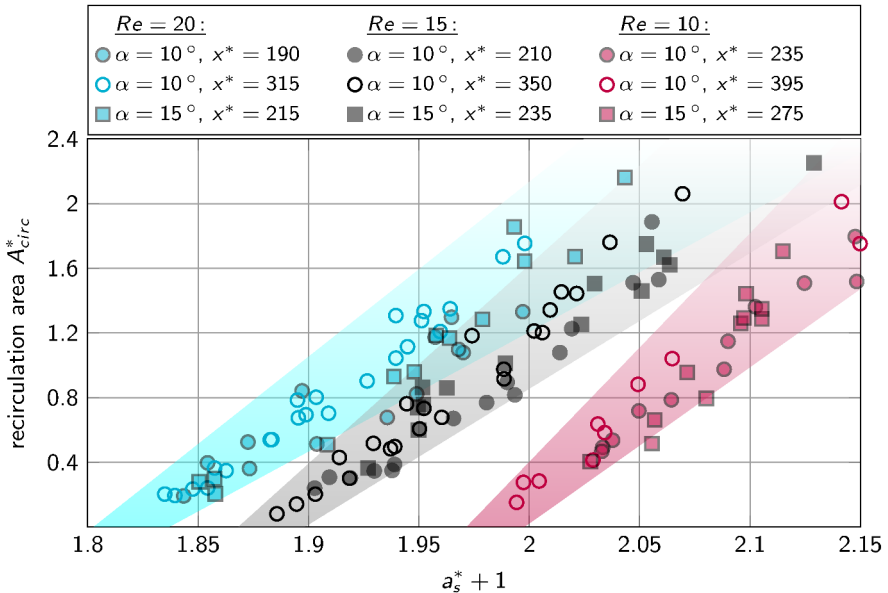

Figure 4.23: The relative size A^*_{circ} vs $a^*_s + 1$: The onset of the recirculation area depends on the Reynolds number of the basic flow, but neither on the inclination angle nor on the measurement position in stream wise direction. For better clarity, error bars were forgone in this plot. Reproduced with permission from [98]. ©2015, AIP Publishing LLC.

wise direction, as previously demonstrated for $Re = 15$. It is influenced by the Reynolds number: For the same amplitude (e.g. $a_s^* + 1 = 2.00$) of the solitary wave, but different Reynolds numbers of the basic flow, the size of the recirculation areas differs. Consequently, the critical wave amplitude for the onset of the recirculation area a_{crit}^* depends on the Reynolds number and can be extracted from figure 4.23: $a_{crit}^*(Re = 10) = 0.98 \pm 0.02$, $a_{crit}^*(Re = 15) = 0.88 \pm 0.02$, $a_{crit}^*(Re = 20) = 0.82 \pm 0.02$.

The dependency of the solitary wave's velocity on its amplitude was measured and plotted in figure 4.18 for $Re = 15$ and $\alpha = 10°$. In order to work with a similar model as proposed by Alekseenko et al. [81], a parabolic function was fitted through these data:

$$v_s^* = 1.07 a_s^{*2} + 1.91. \tag{4.29}$$

In a first approximation, the velocity of a fluid particle at the free surface peak of a solitary wave is taken as:

$$u^*(a_s^*) = (a_s^* + 1)^2. \tag{4.30}$$

A recirculation area appears, if the velocity of a particle at the free surface is at least equal to the wave velocity:

$$v_s^* \leq u^*(a_s^*), \tag{4.31}$$
$$1.07 a_s^{*2} + 1.91 \leq (a_s^* + 1)^2, \tag{4.32}$$
$$\Rightarrow a_s^* \geq 0.46. \tag{4.33}$$

The critical amplitude which was extracted from figure 4.23, was $a_{crit}^*(Re = 15) = 0.88 \pm 0.02$. The discrepancy of the calculated value to the measured one has the following reasons: Firstly, the parabolic models that were assumed for both the velocity of the wave and the fluid at its free surface are not very accurate for solitary waves with a front as steep as the ones present in this study. Secondly, the recirculation area does not appear underneath the highest point of the wave, but directly behind its front (figures 4.19 and 4.20). That means that the fastest fluid particle is not located at the wave's peak, but somewhere in the front. So the actual point, where the recirculation area appears first, lies

lower than the wave height defined in figure 4.16. The exact position of this point could not be determined from the measurements.

It was proven, that recirculation areas appear, if a wave's amplitude exceeds a certain threshold which does neither depend on the distance from the inlet, the initial conditions, nor on the inclination angle of the substrate. The critical amplitude does change with the basic flow's Reynolds number.

5 Conclusions

The dissertation at hand dealt with the dynamics of waves that appear at the free surface of two-dimensional gravity-driven viscous film flows. New measurements were presented and compared to existing theoretical models and results from the literature. The focus was set to two special cases: The dynamics of continuous waves over different substrate topographies and the dynamics of solitary waves over a flat substrate. Both were measured by similar experimental setups that were described in chapter 2. The streamlines underneath large solitary waves were also portrayed, to reveal the existence of recirculation areas underneath these waves.

5.1 Continuous wave dynamics

The dynamics of the continuous waves were measured systematically for four different substrate topographies (figure 2.2): flat (called S_0), sinusoidal (S_1), saw-tooth-like (S_2) and rectangular (S_3). Both the inclination angle α of the substrates and the volume flux $\dot{V}$ of the Newtonian oil *Elbesil 100* through the flow circuit (figure 2.1) were kept constant at $\alpha = 10\,^\circ$ and $\dot{V} = 140\,\mathrm{cm^3/s}$, respectively. With equations 2.1 and 2.6, the Reynolds number Re could be calculated: $Re = 11.9$. A wave generator at the inlet of the channel produced continuous waves by the sinusoidal up and down movement of a paddle (equation 2.7). Seven different paddle frequencies between $1.0\,\mathrm{Hz}$ and $5.0\,\mathrm{Hz}$ and three different paddle amplitudes between $0.25\,\mathrm{mm}$ and $4.0\,\mathrm{mm}$ generated waves of different wave numbers and wave amplitudes.

First, the experiments were validated by comparing the results of the measurements of waves in the linear regime over the flat substrate to results obtained by solving the Orr-Sommerfeld equation (equation 3.15) numerically. Waves were defined as linear, as long as their amplitude to film thickness ratio was

smaller than 0.04 and as long as their shape remained harmonic. When these criteria were fulfilled, it was possible to fit a sinusoidal function with an exponentially growing amplitude (equation 4.9) to the measured wave shapes (figure 4.2). From the fitting parameters, the exponential growth rate, the wave number and the phase velocity could be extracted and compared to the numerical results (figure 4.3). It was shown that the measured and calculated phase velocities are equal, but the growth rates differ. The reason for the difference is as follows: For the derivation of the Orr-Sommerfeld equation, the amplitude of the waves was set to exactly zero, while in the experiments, a finite amplitude had to be present. Considering this, the validation of the experimental setup for the measurement of wave dynamics was successful.

Staying in the linear regime, the influence of the substrate's undulations was analyzed next and compared to the flat substrate. The waves over the undulated substrates (figures 4.5 and 4.6) exhibited a superposition between the steady waves, provoked by the substrate undulations, and the unsteady free surface waves. If the contributions of the steady waves were ignored, it was again possible to fit equation 4.9 to the measured wave shapes and to compare the growth rates and phase velocities of the waves over the different substrates (figure 4.7). It was displayed that the growth rates were much higher for the undulated substrates compared to the flat substrate. The exact shape of the undulation played only a minor role. The phase velocity of the waves over the undulated substrates was much lower than for the flat one. Again, the exact nature of the undulation had only a minor influence. The qualitative behavior of the growth rate and the phase velocity was similar for all topographies.

When the waves were outside the linear regime, nonlinear effects altered their evolution significantly (figures 4.8 and 4.9). They changed their shape from sinusoidal to saw-tooth like, by transferring energy to higher harmonics of their initial wave number. If these higher harmonic wave numbers lay beyond the critical one, they were damped. This led to an equilibrium between the amplification of the first harmonic (which lay below the critical wave number) and energy transfer to higher harmonics. Thus a saturation state will eventually be reached for all nonlinear waves (figure 4.12). What stood out for the flat substrate was the fact that for the neutral wave number that was calculated from the Orr-Sommerfeld equation, the saturation amplitude was zero. But

the growth rate at this point was already significantly negative. That means, in this case it was better to define the neutral wave number experimentally by the lowest wave number whose saturation amplitude became zero, rather than by the wave number whose growth rate was zero. The saturation state differed both quantitatively and qualitatively between the flat and the undulated substrates. The saturation amplitude was about six times higher for the waves over undulated substrates. Also the saturation state of the waves over the flat substrate was a true steady state in a coordinate system that moved with the waves' velocity. But due to the undulations, a true steady state could not be reached for waves over the other topographies.

5.2 Solitary wave dynamics

The solitary waves analyzed in this dissertation were fundamentally different from most studies in the literature: Instead of producing regular wave trains, exactly one wave was generated at the channel's inlet (equation 4.18). Accordingly, the waves were able to attune freely not only in the direction perpendicular to the substrate, but also in the direction parallel to it. Only the flat substrate was used for this case and the inclination angle was set to $\alpha = 10\,^{\circ}$. The volume flux and temperature of the oil *Elbesil 65* in the flow circuit (figure 2.1) were held constant, so that the Reynolds number was also constant at $Re = 15.0$. Eight different paddle periods between 1000 ms and 125 ms and four different paddle amplitudes between 0.05 mm and 4.0 mm generated different initial solitary waves.

Regarding the waves' shape qualitatively in figures 4.14 through 4.16, a couple of observations were made: Generally, the waves grew in height and the front of the waves steepened, until it was almost perpendicular to the substrate. After the depression area that followed the main wave, a second wave developed which was called a "parasitic wave". This parasitic wave had to be much slower than the solitary wave because of the preceding depression area and its much lower film thickness. Due to the low surface tension of the *Elbesil 65* (table 2.1), no capillary ripples were observed. A special case was made for the longest solitary waves: In the first stage of figure 4.14, the wave had a long and flat top. In the later stages, this wave broke up into two waves with a small depression

area in between. The break-up is also visible in figures 4.15 and 4.16, but less pronounced. This phenomenon was explained by considering the flat initial state of the solitary wave as a film flow with a higher film thickness than the waveless state. Since this film flow was unstable, waves had to appear on top of the flat solitary wave. The length of the wave was finite and hence only one dent appeared and split the solitary wave. If the wave had been longer, the solitary wave should have broken up into more parts. The waves with lower initial lengths were too short to be considered as a flat film flow and so did not exhibit a break-up.

In the quantitative assessment of the solitary waves, the focus was put on the main wave and not the parasitic wave or the second part of the broken-up wave. Figure 4.16 shows the definition of its key parameters: Its amplitude, its length and its position, from which its velocity was derived. Figure 4.17 displays their development down the channel. It was demonstrated that the wave's amplitude and length did not develop independently, but a shortening/lengthening of the wave gave rise to a increase/decrease of the wave's amplitude. As soon as the length became constant, the amplitude tended to the same value for all waves. Also the wave's velocity depended nonlinearly on its amplitude. In a first approximation, a quadratic function could be fitted to the measured data (figure 4.18).

In order to gain more insight on the dynamics of solitary waves, the streamlines underneath large solitary waves were portrayed in a reference frame that moved with the wave's speed. The wave was considered as steady in that reference frame during the short recording time. It was proven experimentally that recirculation areas underneath sufficiently large waves appear (figures 4.19 and 4.20). The critical wave amplitude for their appearance did neither depend on the initial conditions of the wave, on the measurement position in stream wise direction (figure 4.21), nor on the inclination angle of the substrate (figure 4.22). It did depend on the Reynolds number (figure 4.23).

5.3 Summary and outlook

Overall, the present work presents new experimental results on the dynamics of free surface waves on gravity-driven film flows. Especially the influence of substrate topographies on continuous waves and the behavior of solitary waves was scrutinized systematically. In the study of the continuous wave dynamics, only a small parameter space was covered by the experiments that were analyzed, i.e. the wavelength, amplitude and inclination angle of the substrate and the Reynolds number were kept constant. So changing one of these parameters, e.g. the wavelength of the undulations, should give further insight into the continuous wave dynamics. Complementary numerical calculations of the full Navier-Stokes equations will also help in understanding the mechanisms behind the measured results and also a larger parameter space can be covered by numerical investigations. Concerning the solitary wave dynamics, the recirculation areas underneath large solitary waves are of special interest to heat and mass transfer applications. There, it is crucial to identify the exact parameters that influence the onset of these recirculation areas.

List of symbols

symbol (unit)	description	page list
Δ	Error of a value	23, 66, 72
α (°)	Inclination angle	12, 17, 18, 20, 36, 39–43, 45, 61, 71–76, 79, 81
ϵ	Magnitude of the linear disturbance	37, 38, 42, 49
η (mPas)	Dynamic viscosity	20, 21, 91
κ^*	Curverture of the free surface, dimensionless	39
λ_{blue} (m)	Wavelength of the blue laser	23
λ_s (m)	Solitary wave's full length at half maximum	30, 33
λ_s^*	Solitary wave's full length at half maximum, dimensionless	33, 66, 67
ν (m^{2}s^{-1})	Kinematic viscosity	17, 20–23
ψ	Stream function	38–41
ρ (kgm^{-3})	Density	20–22, 35, 91
σ (Nm^{-1})	Surface tension	17, 20–22, 91
τ (s)	Phase difference	28–30
θ (°C)	Temperature	21, 22, 45, 61, 91, 93
φ (rad)	Phase difference	28, 29
a_c (m)	Continuous wave's amplitude	26, 33, 47
a_c^*	Continuous wave's amplitude, dimensionless	33, 47
A_{circ} (m^2)	Size of the recirculation area	69, 70, 72

symbol (unit)	description	page list
A^*_{circ}	Size of the recirculation area, dimensionless	72–75
a^*_{crit}	Critical amplitude for the onset of recirculation areas, dimensionless	76
a_p (m)	Paddle's position	26, 61, 62
$a_{p,0}$ (m)	Paddle's amplitude	26, 46–48, 50–57, 59, 61–63, 65–67, 70–73, 92, 93
a_s (m)	Solitary wave's amplitude	30, 33, 69, 70, 72
a^*_s	Solitary wave's amplitude, dimensionless	33, 66–68, 70, 72–76
a^*_{sat}	Saturation amplitude, dimensionless	56, 58, 59
a_{sub} (m)	Substrate's amplitude	18
b^*	Exponential growth rate of linear waves, dimensionless	39–41, 47–49, 53, 58
c^*	Complex wave velocity, dimensionless	37–41
d_{loc} (m)	Local film thickness	23
d_n (m)	Nusselt film thickness	20, 22, 33, 35, 45–47, 56, 58, 61–63, 70–74
$\mathcal{F}$	Fast Fourier Transformation	28
f_p (s^{-1})	Paddle's frequency	26, 28, 30, 46, 47, 50–52, 56, 57
g (ms^{-2})	Gravity constant	20, 22
$\hat{h}$	Linear free surface displacement, dimensionless	37–39
h (m)	Free surface's non-steady shape	26, 27, 30
h_0 (m)	Basic flow's free surface shape	17, 23–27, 30, 91
h_c (m)	Continuous wave's shape	26–30, 33, 47, 50, 91

symbol (unit)	description	page list
h_c^*	Continuous wave's shape, dimensionless	33, 37–39, 42, 43, 47, 48, 51, 52, 54, 55
h_s (m)	Solitary wave's shape	30, 31, 33, 63, 91
h_s^*	Solitary wave's shape, dimensionless	33, 63, 65, 92, 93
$\mathcal{I}$	Imaginary part of a complex number	28, 39–41
k_c (m^{-1})	Continuous wave's wave number	26, 33
k_c^*	Continuous wave's wave number, dimensionless	33, 37–44, 47–49, 52, 53, 56, 58
Ka	Kapitza number	22, 25, 39–43, 47, 48, 50–52, 54, 55, 63, 65, 70, 91–93
l_{blue} (m)	Line length of the blue laser	24
L_{sub} (m)	Substrate's wavelength	18, 27
l_{sub} (m)	Substrate's total length	18
$\vec{m}$	Tangential vector of the free surface	38, 39
$\vec{n}$	Normal vector of the free surface	38, 39
N_{sub}	Substrate's number of undulations	18, 27, 28, 30
$\hat{p}$	Linear pressure disturbance, dimensionless	37–39
p (kgm^{-2}s^{-2})	Pressure distribution	35
P^*	Pressure distribution of the basic flow, dimensionless	36, 37
p^*	Pressure distribution, dimensionless	35, 37
P_{blue} (W)	Power of the blue laser	23
$\dot{Q}$ (m^{2}s^{-1})	Two-dimensional flow rate	17, 19, 22, 23
$\mathcal{R}$	Real part of a complex number	28, 39, 40

symbol (unit)	description	page list
Re	Reynolds number	22, 23, 25, 36, 38–43, 45–55, 61, 63, 65, 71–74, 76, 79, 81, 91–93
Re_c	Critical Reynolds number	12, 40, 41, 43
S_0	Flat substrate	18, 30, 31, 45–50, 52–54, 56–59, 61, 79, 91
S_1	Sinusoidal substrate	18, 25, 27, 29, 45, 46, 50–52, 54, 56, 57, 59, 60, 79, 91
S_2	Saw-tooth-like substrate	18, 45, 46, 51, 52, 55, 60, 79
S_3	Rectangular substrate	18, 45, 46, 51, 52, 55, 59, 60, 79
t (s)	Time	26–31, 35, 47, 50, 61, 62, 69, 91
$\vec{t}$	Stress vector	38, 39
t^*	Time, dimensionless	35, 37–39, 42, 43, 47, 48, 51, 52, 54, 55, 63, 65, 66, 92, 93
$t_{2,3}$ (s)	Delay between recordings at position 2 and 3	28
T_p (s)	Paddle's period	30, 61–64, 70–73
$\hat{u}$	The x-component of the linear velocity disturbance, dimensionless	37–39
u (ms^{-1})	The x-component of the velocity vector	22
$\vec{u}$ (ms^{-1})	Velocity vector	17, 35
U^*	The x-component of the basic flow's velocity field, dimensionless	35–38

symbol (unit)	description	page list
u^*	The x-component of the velocity vector, dimensionless	37, 38, 43, 44, 76
$\vec{u}^*$	Velocity vector, dimensionless	35, 36, 38
u_{loc} (ms^{-1})	Local free surface velocity	23
u_s (ms^{-1})	Nusselt free surface velocity	20, 22, 33, 35, 40, 45, 46, 61, 70–74
$\dot{V}$ (m^{3}s^{-1})	Three-dimensional volume flux	17, 19, 20, 23, 45, 61, 79, 91
v_c (ms^{-1})	Continuous wave's phase velocity	26, 33, 40
v_c^*	Continuous wave's phase velocity, dimensionless	33, 39, 47–49, 53
v_s (ms^{-1})	Solitary wave's phase velocity	30–33, 69, 70, 72
v_s^*	Solitary wave's phase velocity, dimensionless	33, 66–68, 76
$\hat{w}$	The z-component of the linear velocity disturbance, dimensionless	37–39
w^*	The z-component of the velocity vector, dimensionless	37, 38, 43
w_{blue} (m)	Line width of the blue laser	24
w_{sub} (m)	Substrate's width	18–20, 23
We	Weber number	42, 43
x (m)	The x-coordinate	17, 18, 23–31, 35, 36, 47, 50, 60, 69, 72, 74, 75, 91
x' (m)	The x'-coordinate in the moving coordinate system	31, 69
x^*	The x-coordinate, dimensionless	35–39, 42, 43, 47, 48, 51, 52, 54–57, 63, 65, 66, 68, 71–74, 92, 93
x_c (m)	Image's size in x-direction	27
y (m)	The y-coordinate	18, 19, 24, 31, 37, 69

symbol (unit)	description	page list
z (m)	The z-coordinate	17, 24, 31, 35, 36, 69
z^*	The z-coordinate, dimensionless	35–41, 43, 44, 68

List of figures

List of tables

Bibliography

[1] I. Luca, K. Hutter, Y.C. Tai, and C.Y. Kuo, "A hierarchy of avalanche models on arbitrary topography", *Acta Mechanica* **205**, 121–149 (2009).

[2] R. Greve and H. Blatter, *Dynamics of Ice Sheets and Glaciers*, Springer-Verlag, Berlin, Heidelberg, 2009.

[3] S.F. Kistler and P.M. Schweizer, *Liquid Film Coating*, Chapman and Hall, New York, 1997.

[4] S.J. Weinstein and K.J. Ruschak, "Coating Flows", *Annual Review of Fluid Mechanics* **36**, 29–53 (2004).

[5] G. Gugler, R. Beer, and M. Mauron, "Operative limits of curtain coating due to edges", *Chemical Engineering and Processing: Process Intensification* **50**, 462–465 (2011).

[6] R.L. Webb, *Principles of Enhanced Heat Transfer*, Wiley, New York, 1994.

[7] A.A. Alhusseini, K. Tuzla, and J.C. Chen, "Falling film evaporation of single component liquids", *International Journal of Heat and Mass Transfer* **41**, 1623–1632 (1998).

[8] W. Nusselt, "Die Oberflächenkondensation des Wasserdampfes", *VDI Zeitschrift* **60**, 541–546 (1916).

[9] A. Haas, T. Pollak, and N. Aksel, "Side wall effects in thin gravity-driven film flow – steady and draining flow", *Physics of Fluids* **23**, 062107 (2011).

[10] M. Scholle and N. Aksel, "An exact solution of visco-capillary flow in an inclined channel", *Zeitschrift für Angewandte Mathematik und Physik ZAMP* **52**, 749–769 (2001).

[11] M. Scholle and N. Aksel, "Thin film limit and film rupture of the visco-capillary gravity-driven channel flow", *Zeitschrift für Angewandte Mathematik und Physik ZAMP* **54**, 517–531 (2003).

[12] C. Pozrikidis and S.T. Thoroddsen, "The deformation of a liquid film flowing down an inclined plane wall over a small particle arrested on the wall", *Physics of Fluids A* **3**, 2546–2558 (1991).

[13] S. Kalliadasis, C. Bielarz, and G.M. Homsy, "Steady free-surface thin film flows over topography", *Physics of Fluids* **12**, 1889–1898 (2000).

[14] M. Hayes, S.B.G. O'Brien, and J.H. Lammers, "Greens function for steady flow over a small two-dimensional topography", *Physics of Fluids* **12**, 2845–2858 (2000).

[15] A. Mazouchi and G.M. Homsy, "Free surface Stokes flow over topography", *Physics of Fluids* **13**, 2751–2761 (2001).

[16] M.M.J. Decré and J.-C. Baret, "Gravity-driven flows of viscous liquids over two-dimensional topographies", *Journal of Fluid Mechanics* **487**, 147–166 (2003).

[17] N. Aksel, "Influence of the capillarity on a creeping film flow down an inclined plane with an edge", *Archive of Applied Mechanics* **70**, 81–90 (2000).

[18] M. Scholle and N. Aksel, "A general free surface rule for Stokes flow of fluid films over obstacles", *Acta Mechanica* **191**, 155–159 (2007).

[19] C. Pozrikidis, "The flow of a liquid film along a periodic wall", *Journal of Fluid Mechanics* **188**, 275–300 (1988).

[20] V. Bontozoglou and G. Papapolymerou, "Laminar film flow down a wavy incline", *International Journal of Multiphase Flow* **23**, 69–79 (1997).

[21] M. Scholle, A. Wierschem, and N. Aksel, "Creeping Newtonian film flow down an inclined wavy plane. Part I", *ZAMM – Journal of Applied Mathematics and Mechanics / Zeitschrift für Angewandte Mathematik und Mechanik* **81**, 487–488 (2001).

[22] Y.Y. Trifonov, "Viscous liquid film flows over a periodic surface", *International Journal of Multiphase Flow* **24**, 1139–1161 (1999).

[23] A. Wierschem, V. Bontozoglou, C. Heining, H. Uecker, and N. Aksel, "Linear resonance in viscous films on inclined wavy planes", *International Journal of Multiphase Flow* **34**, 580–589 (2008).

[24] C. Heining, V. Bontozoglou, N. Aksel, and A. Wierschem, "Nonlinear resonance in viscous films on inclined wavy planes", *International Journal of Multiphase Flow* **35**, 78–90 (2009).

[25] M.I. Pak and G.H. Hu, "Numerical investigations on vortical structures of viscous film flows along periodic rectangular corrugations", *International Journal of Multiphase Flow* **37**, 369–379 (2011).

[26] M. Vlachogiannis and V. Bontozoglou, "Experiments on laminar film flow along a periodic wall", *Journal of Fluid Mechanics* **457**, 133–456 (2002).

[27] K. Argyriadi, M. Vlachogiannis, and V. Bontozoglou, "Experimental study of inclined film flow along periodic corrugations: The effect of wall steepness", *Physics of Fluids* **18**, 012102 (2006).

[28] M Schörner, D. Reck, and N. Aksel, "Does the topography's specific shape matter in general for the stability of film flows?", *Physics of Fluids* **27**, 042103 (2015).

[29] A. Wierschem and N. Aksel, "Hydraulic jumps and standing waves in gravity-driven flows of viscous liquids in wavy open channels", *Physics of Fluids* **16**, 3868–3877 (2004).

[30] M. Sellier, "Substrate design or reconstruction from free surface data for thin film flows", *Physics of Fluids* **20**, 062106 (2008).

[31] C. Heining and N. Aksel, "Bottom reconstruction in thin-film flow over topography: Steady solution and linear stability", *Physics of Fluids* **21**, 083605 (2009).

[32] C. Heining, "Velocity field reconstruction in gravity-driven flow over unknown topography", *Physics of Fluids* **23**, 032101 (2011).

[33] C. Heining, T. Pollak, and M. Sellier, "Flow domain identification from free surface velocity in thin inertial films", *Journal of Fluid Mechanics* **720**, 338–356 (2013).

[34] A. Wierschem, M. Scholle, and N. Aksel, "Vortices in film flow over strongly undulated bottom profiles at low Reynolds numbers", *Physics of Fluids* **15**, 426–435 (2003).

[35] M. Scholle, A. Wierschem, and N. Aksel, "Creeping films with vortices over strongly undulated bottoms", *Acta Mechanica* **168**, 167–193 (2004).

[36] A. Wierschem and N. Aksel, "Influence of inertia on eddies created in films creeping over strongly undulated substrates", *Physics of Fluids* **16**, 4566–4574 (2004).

[37] M. Scholle, A. Haas, N. Aksel, M.C.T. Wilson, H.M. Thompson, and P.H. Gaskell, "Eddy genesis and manipulation in plane laminar shear flow", *Physics of Fluids* **21**, 073602 (2009).

[38] M. Scholle, A. Haas, N. Aksel, M.C.T. Wilson, H.M. Thompson, and P.H. Gaskell, "Competing geometric and inertial effects on local flow structure in thick gravity-driven fluid films", *Physics of Fluids* **20**, 123101 (2008).

[39] M. Scholle, A. Haas, N. Aksel, H.M. Thompson, R.W. Hewson, and P.H. Gaskell, "The effect of locally induced flow structure on global heat transfer for plane laminar shear flow", *International Journal of Heat and Fluid Flow* **30**, 175–185 (2009).

[40] A. Wierschem, T. Pollak, C. Heining, and N. Aksel, "Suppression of eddies in films over topography", *Physics of Fluids* **22**, 113603 (2010).

[41] P.L. Kapitza and S.P. Kapitza, "Wave Flow of Thin Layers of a Viscous Liquid", *Zh. Eksp. Teor. Fiz.* **18**, 3–28 (1948).

[42] P.L Kapitza, "Wave Flow of Thin Viscous Liquid Layers", *Zh. Eksp. Teor. Fiz.* **19**, 3–28 (1948).

[43] C.S. Yih, "Stability of liquid flow down an inclined plane", *Physics of Fluids* **6**, 321–334 (1963).

[44] T.B. Benjamin, "Wave formation in laminar flow down an inclined plane", *Journal of Fluid Mechanics* **2**, 554–573 (1957).

[45] W.M'F. Orr, "The Stability or Instability of the Steady Motions of a Perfect Liquid and of a Viscous Liquid. Part I: A Perfect Liquid", *Proceedings of the Royal Irish Academy. Section A: Mathematical and Physical Sciences* **27**, 9–68 (1907).

[46] W.M'F. Orr, "The Stability or Instability of the Steady Motions of a Perfect Liquid and of a Viscous Liquid. Part II: A Viscous Liquid", *Proceedings of the Royal Irish Academy. Section A: Mathematical and Physical Sciences* **27**, 69–138 (1907).

[47] A. Sommerfeld, "Ein Beitrag zur hydrodynamischen Erklärung der turbulenten Flüssigkeitsbewegungen", *Proceedings of the 4th International Congress of Mathematicians* **3**, 116–124 (1908).

[48] J. Liu, J.D. Paul, and J.P. Gollub, "Measurements of the primary instabilities of film flows", *Journal of Fluid Mechanics* **250**, 69–101 (1993).

[49] M. Vlachogiannis, A. Samandas, V. Leontidis, and V. Bontozoglou, "Effect of channel width on the primary instability of inclined film flow", *Physics of Fluids* **22**, 012106 (2010).

[50] A. Georgantaki, J. Vatteville, M. Vlachogiannis, and V. Bontozoglou, "Measurements of liquid film flow as a function of fluid properties and channel width: Evidence for surface-tension-induced long-range transverse coherence", *Physical Review E* **84**, 026325 (2011).

[51] T. Pollak, A. Haas, and N. Aksel, "Side wall effects on the instability of thin gravity-driven films – From long-wave to short-wave instability", *Physics of Fluids* **23**, 094110 (2011).

[52] A. Wierschem and N. Aksel, "Instability of a liquid film flowing down an inclined wavy plane", *Physica D* **186**, 221–237 (2003).

[53] A. Wierschem, C. Lepski, and N. Aksel, "Effect of long undulated bottoms on thin gravity-driven films", *Acta Mechanica* **179**, 41–66 (2005).

[54] L.A. Dávalos-Orozco, "Nonlinear instability of a thin film flowing down a smoothly deformed surface", *Physics of Fluids* **19**, 074103–1 – 074103–8 (2007).

[55] Y.Y. Trifonov, "Stability and nonlinear wavy regimes in downward film flows on a corrugated surface", *Journal of Applied Mechanics and Technical Physics* **48**, 91–100 (2007).

[56] Y.Y. Trifonov, "Stability of a viscous liquid film flowing down a periodic surface", *International Journal of Multiphase Flow* **33**, 1186–1204 (2007).

[57] Y.Y. Trifonov, "Stability and bifurcations of the wavy film flow down a vertical plate: the results of integral approaches and full-scale computations", *Fluid Dynamics Research* **44**, 031418 (2012).

[58] S.J.D. D'Alessio, J.P. Pascal, and H.A. Jasmine, "Instability in gravity-driven flow over uneven surfaces", *Physics of Fluids* **21**, 062105 (2009).

[59] D. Tseluiko, M.G. Blyth, and D.T. Papageorgiou, "Stability of film flow over inclined topography based on a long-wave nonlinear model", *Journal of Fluid Mechanics* **729**, 638–671 (2013).

[60] C. Heining and N. Aksel, "Effects of inertia and surface tension on a power-law fluid flowing down a wavy incline", *International Journal of Multiphase Flow* **36**, 847–857 (2010).

[61] T. Pollak and N. Aksel, "Crucial flow stabilization and multiple instability branches of gravity-driven films over topography", *Physics of Fluids* **25**, 024103 (2013).

[62] Y.Y. Trifonov, "Stability of a film flowing down an inclined corrugated plate: The direct Navier-Stokes computations and Floquet theory", *Physics of Fluids* **26**, 114101 (2014).

[63] M. Schörner, D. Reck, and N. Aksel, "Stability phenomena far beyond the Nusselt flow – Revealed by experimental asymptotics", *Physics of Fluids* **28**, 022102 (2016).

[64] Z. Cao, M. Vlachogiannis, and V. Bontozoglou, "Experimental evidence for a short-wave global mode in film flow along periodic corrugations", *Journal of Fluid Mechanics* **718**, 304–320 (2013).

[65] S.P. Lin, "Finite-amplitude stability of a parallel flow with a free surface", *Journal of Fluid Mechanics* **36**, 113–126 (1969).

[66] H.-C. Chang, E.A. Demekhin, and D.I. Kopelevich, "Nonlinear evolution of waves on a vertically falling film", *Journal of Fluid Mechanics* **250**, 433–480 (1993).

[67] D.J. Benney, "Long waves on liquid films", *Journal of Mathematics and Physics* **45**, 150–155 (1966).

[68] B. Gjevik, "Occurrence of finite amplitude surface waves on falling liquid films", *Physics of Fluids* **13**, 1918–1925 (1970).

[69] W.B. Krantz and S.L. Goren, "Finite-amplitude, long waves on liquid films flowing down a plane", *Industrial & Engineering Chemistry Fundamentals* **9**, 107–113 (1970).

[70] Y.Y. Trifonov and O.Y. Tsvelodub, "Nonlinear waves on the surface of a falling liquid film. Part 1. Waves of the first family and their stability", *Journal of Fluid Mechanics* **229**, 531–554 (1990).

[71] L.Q. Yu, F.K. Wasden, A.E. Dukler, and V. Balakotaiah, "Nonlinear evolution of waves on falling films at high Reynolds numbers", *Physics of Fluids* **7**, 1886–1902 (1995).

[72] C. Ruyer-Quil and P. Manneville, "Improved modeling of flows down inclined planes", *The European Physical Journal B – Condensed Matter and Complex Systems* **15**, 357–369 (2000).

[73] P. Rosenau and A. Oron, "Evolution and breaking of liquid film flowing on a vertical cylinder", *Physics of Fluids A* **1**, 1763–1766 (1989).

[74] A. Oron and O. Gottlieb, "Nonlinear dynamics of temporally excited falling liquid films", *Physics of Fluids* **14**, 2622–2636 (2002).

[75] H.-C. Chang and E.A. Demekhin, *Complex Wave Dynamics on Thin Films*, Elsevier, Amsterdam, 2002.

[76] N.A. Malamataris, M. Vlachogiannis, and V. Bontozoglou, "Solitary waves on inclined films: Flow structure and binary interactions", *Physics of Fluids* **14**, 1082–1094 (2002).

[77] K. Argyriadi, K. Serifi, and V. Bontozoglou, "Nonlinear dynamics of inclined films under low-frequency forcing", *Physics of Fluids* **16**, 2457–2468 (2004).

[78] T. Nosoko and A. Miyara, "The evolution and subsequent dynamics of waves on a vertically falling liquid film", *Physics of Fluids* **16**, 1118–1126 (2004).

[79] J. Liu and J.P. Gollub, "Solitary wave dynamics of film flows", *Physics of Fluids* **6**, 1702–1712 (1994).

[80] M. Vlachogiannis and V. Bontozoglou, "Observations of solitary wave dynamics of film flows", *Journal of Fluid Mechanics* **435**, 191–215 (2001).

[81] S.V. Alekseenko, V.Y. Nakoryakov, and B.G. Pokusaev, "Wave formation on a vertical falling liquid film", *AIChE Journal* **31**, 1446–1460 (1985).

[82] S. Chakraborty, P.K. Nguyen, C. Ruyer-Quil, and V. Bontozoglou, "Extreme solitary waves on falling liquid films", *Journal of Fluid Mechanics* **745**, 564–591 (2014).

[83] H.-C. Chang, E. Demekhin, and E. Kalaidin, "Interaction dynamics of solitary waves on a falling film", *Journal of Fluid Mechanics* **294**, 123–154 (1995).

[84] N.A. Malamataris and V. Balakotaiah, "Flow structure underneath the large amplitude waves of a vertically falling film", *AIChE Journal* **54**, 1725–1740 (2008).

[85] C.E. Meza and V. Balakotaiah, "Modeling and experimental studies of large amplitude waves on vertically falling films", *Chemical Engineering Science* **63**, 4704–4734 (2008).

[86] A. Miyara, "Numerical simulation of wavy liquid film flowing down on a vertical wall and an inclined wall", *International Journal of Thermal Sciences* **39**, 1015–1027 (2000).

[87] A. Miyara, "Numerical analysis on flow dynamics and heat transfer of falling liquid films with interfacial waves", *Heat and Mass Transfer* **35**, 298–306 (1999).

[88] H.S. Brown, I.G. Kevrekidis, A. Oron, and P. Rosenau, "Bifurcations and pattern formation in the regularized Kuramoto-Sivashinsky equation", *Physics Letters A* **163**, 299 – 308 (1992).

[89] H.-C. Chang, "Wave evolution on a falling film", *Annual Review of Fluid Mechanics* **26**, 103–136 (1994).

[90] R.V. Craster and O.K. Matar, "Dynamics and stability of thin liquid films", *Reviews of Modern Physics* **81**, 1131–1198 (2009).

[91] J. Liu, J.B. Schneider, and J.P. Gollub, "Three-dimensional instabilities of film flows", *Physics of Fluids* **7**, 55–67 (1995).

[92] C.D. Park and T. Nosoko, "Three-dimensional wave dynamics on a falling film and associated mass transfer", *AIChE Journal* **49**, 2715–2727 (2003).

[93] P. Adomeit and U. Renz, "Hydrodynamics of three-dimensional waves in laminar falling films", *International Journal of Multiphase Flow* **26**, 1183–1208 (2000).

[94] B. Scheid, C. Ruyer-Quil, and P. Manneville, "Wave patterns in film flows: modelling and three-dimensional waves", *Journal of Fluid Mechanics* **562**, 183–222 (2006).

[95] D. Reck and N. Aksel, "Experimental study on the evolution of traveling waves over an undulated incline", *Physics of Fluids* **25**, 102101 (2013).

[96] J. Spurk and N. Aksel, *Fluid Mechanics*, Springer-Verlag, Berlin, Heidelberg, 2008.

[97] Laser Components, `http://www.lasercomponents.com/fileadmin/user_upload/home/Datasheets/lasermodules/fp-405-450-488-lasers.pdf`, 2015 (accessed Oct 02 2015).

[98] D. Reck and N. Aksel, "Recirculation areas underneath solitary waves on gravity-driven film flows", *Physics of Fluids* **27**, 112107 (2015).

[99] Clay Mathematics Institute, `http://www.claymath.org/millennium-problems/navier%E2%80%93stokes-equation`, 2016 (accessed Jan 28 2016).

[100] M. Hermann, *Numerik gewöhnlicher Differentialgleichungen: Anfangs- und Randwertprobleme*, Oldenbourg Wissenschaftsverlag, Berlin, Boston, 2009.

[101] P. Deuflhard, *Newton Methods for Nonlinear Problems*, Springer-Verlag, Berlin, Heidelberg, 2004.

[102] S. Kalliadasis, C. Ruyer-Quil, B. Scheid, and M.G. Velarde, *Falling liquid films*, Springer London, 2012.

[103] S.P. Lin, "Finite amplitude side-band stability of a viscous film", *Journal of Fluid Mechanics* **63**, 417–429 (1974).

[104] A. Oron and O. Gottlieb, "Subcritical and supercritical bifurcations of the first- and second-order Benney equations", *Journal of Engineering Mathematics* **50**, 121–140 (2004).

[105] A. Pumir, P. Manneville, and Y. Pomeau, "On solitary waves running down an inclined plane", *Journal of Fluid Mechanics* **135**, 27–50 (1983).

[106] O. Takeshi, "Surface equation of falling film flows with moderate Reynolds number and large but finite Weber number", *Physics of Fluids* **11**, 3247–3269 (1999).

[107] V.Y. Shkadov, "Solitary waves in a layer of viscous liquid", *Fluid Dynamics* **12**, 52–55 (1977).

[108] A. Oron and C. Heining, "Weighted-residual integral boundary-layer model for the nonlinear dynamics of thin liquid films falling on an undulating vertical wall", *Physics of Fluids* **20**, 082102 (2008).

[109] J. Tihon, K. Serifi, K. Argyriadi, and V. Bontozoglou, "Solitary waves on inclined films: their characteristics and the effects on wall shear stress", *Experiments in Fluids* **41**, 79–89 (2006).

[110] F.K. Wasden and A.E. Dukler, "Insights into the hydrodynamics of free falling wavy films", *AIChE Journal* **35**, 187–195 (1989).

[111] D. Gao, N.B. Morley, and V. Dhir, "Numerical simulation of wavy falling film flow using VOF method", *Journal of Computational Physics* **192**, 624–642 (2003).

[112] W. Rohlfs and B. Scheid, "Phase diagram for the onset of circulating waves and flow reversal in inclined falling films", *Journal of Fluid Mechanics* **763**, 322–351 (2015).

[113] E.S. Benilov and V.N. Lapin, "An example where lubrication theory comes short: hydraulic jumps in a flow down an inclined plate", *Journal of Fluid Mechanics* **764**, 277–295 (2015).

List of journal publications

Daniel Reck and Nuri Aksel.
"Experimental study on the evolution of traveling waves over an undulated incline"
Physics of Fluids, **25**, 102101 (2013).

Mario Schörner, Daniel Reck and Nuri Aksel.
"Does the topography's specific shape matter in general for the stability of film flows?"
Physics of Fluids, **27**, 042103 (2015).

Daniel Reck and Nuri Aksel.
"Recirculation areas underneath solitary waves on gravity-driven film flows"
Physics of Fluids, **27**, 112107 (2015).

Mario Schörner, Daniel Reck and Nuri Aksel.
"Stability phenomena far beyond Nusselt flow – Revealed by experimental asymptotics"
Physics of Fluids, **28**, 022102 (2016).

Mario Schörner, Daniel Reck, Nuri Aksel and Yuri Trifonov.
"Switching between different types of stability isles in films over topographies"
submitted to Physical Review Fluids.

Danksagungen

An dieser Stelle möchte ich mich ganz herzlich bei allen Mitarbeitern des Lehrstuhls für Technische Mechanik und Strömungsmechanik der Universität Bayreuth bedanken, die für ein freundliches, angenehmes und produktives Arbeitsklima gesorgt haben. Insbesondere gilt mein Dank dem Lehrstuhlinhaber Herrn Professor Dr. Nuri Aksel für die exzellente Betreuung meiner Arbeit. Er nahm sich stets Zeit für Diskussionen und seine Anregungen und Denkanstöße waren eine großartige Hilfe bei der Entwicklung, Durchführung und Auswertung von Experimenten sowie bei der Interpretation der Ergebnisse. Außerdem gab er mir die Möglichkeit, an mehreren Fachtagungen teilzunehmen, wobei viele Kontakte zu internationalen Forscherkollegen entstanden. Unter diesen befand sich auch der Zweitgutachter der Dissertation, Professor Dr. Alexander Oron (Technion, Israel Institute of Technology, Haifa). Ich danke Professor Oron vielmals für seine gründliche Begutachtung der Arbeit und seine konstruktiven Verbesserungsvorschläge.

Des Weiteren möchte ich mich für die hervorragende Zusammenarbeit mit meinen Kollegen Dr. Thilo Pollak, Mario Schörner und Markus Dauth bedanken. Bei reichhaltigen Fachdiskussionen wurden Probleme gelöst, Projekte weiterentwickelt und neue Ideen ausgearbeitet. Hervorzuheben ist auch die Unterstützung bei der Durchführung von Experimenten und der Arbeit im Labor durch Marion Märkl, Gabriele Jena, Markus Horn und Stephan Eißner, ohne die ein effizientes wissenschaftliches Arbeiten nicht möglich gewesen wäre. Bedanken will ich mich auch bei Dr. Lutz Heymann für seine Anmerkungen zu meiner Dissertation und Hilfestellungen beim Aufbau von Experimenten, sowie bei Katja Helmrich, die dafür gesorgt hat, dass organisatorische Angelegenheiten immer reibungslos abgewickelt wurden. Danke außerdem an die Mechanikwerkstatt der Universität Bayreuth für die gute Zusammenarbeit und qualitativ hochwertige Fertigung von Versuchskomponenten.

Mein besonderer Dank geht an meine Familie und meine Freundin, die mich immer unterstützt haben, sodass ich sowohl mein Studium als auch diese Arbeit erfolgreich abschließen konnte.

Hiermit versichere ich, dass ich die Dissertation selbstständig verfasst und keine anderen als die von mir angegebenen Quellen und Hilfsmittel benutzt habe.

Ich erkläre, dass ich diese Dissertation nicht bereits zur Erlangung eines akademischen Grades eingereicht habe und dass ich nicht bereits diese oder eine gleichartige Doktorprüfung endgültig nicht bestanden habe.

Des Weiteren erkläre ich, dass ein gewerblicher Promotionsberater bzw. Promotionsvermittler weder bisher in Anspruch genommen wurde noch künftig in Anspruch genommen wird.

_____   _____
(Ort, Datum)   (Dipl.-Phys. Daniel Reck)